

Unraveling emission line galaxy conformity at $z \sim 1$ with DESI early data

Sihan Yuan^{1,2*}, Risa H. Wechsler^{1,2,3}, Yunchong Wang¹, Mithi A.C. de los Reyes^{1,4}, Justin Myles^{1,5}, Antoine Rocher⁶, Boryana Hadzhiyska⁸, Jessica Nicole Aguilar⁸, Steven Ahlen⁹, David Brooks¹¹, Todd Claybaugh⁸, Shaun Cole¹², Axel de la Macorra¹³, Jaime E. Forero-Romero¹⁴, Satya Gontcho A Gontcho⁸, Julien Guy⁸, Klaus Honscheid^{15,16}, Theodore Kisner⁸, Michael Levi⁸, Marc Manera¹⁷, Aaron Meisner¹⁸, Ramon Miquel^{17,19}, John Moustakas²⁰, Jundan Nie²¹, Nathalie Palanque-Delabrouille^{8,28}, Claire Poppett^{8,22}, Mehdi Rezaie²³, Ashley J. Ross¹⁶, Graziano Rossi²⁴, Eusebio Sanchez²⁵, Michael Schubnell²⁶, Hee-Jong Seo²⁷, Gregory Tarlé²⁶, Benjamin Alan Weaver¹⁸, and Zhimin Zhou²¹

The authors' affiliations are shown in Appendix A

Accepted XXX. Received YYY; in original form ZZZ

ABSTRACT

Emission line galaxies (ELGs) are now the preeminent tracers of large-scale structure at $z > 0.8$ due to their high density and strong emission lines, which enable accurate redshift measurements. However, relatively little is known about ELG evolution and the ELG–halo connection, exposing us to potential modeling systematics in cosmology inference using these sources. In this paper, we propose a physical picture of ELGs and improve ELG–halo connection modeling using a variety of observations and simulated galaxy models. We investigate DESI-selected ELGs in COSMOS data, and infer that ELGs are rapidly star-forming galaxies with a large fraction exhibiting disturbed morphology, implying that many of them are likely to be merger-driven starbursts. We further postulate that the tidal interactions from mergers lead to correlated star formation in central–satellite ELG pairs, a phenomenon dubbed “conformity.” We argue for the need to include conformity in the ELG–halo connection using galaxy models such as ILLUSTRISTNG, and by combining observations such as the DESI ELG auto-correlation, ELG cross-correlation with Luminous Red Galaxies (LRGs), and ELG–cluster cross-correlation. We also explore the origin of conformity using the UniverseMachine model and elucidate the difference between conformity and the well-known galaxy assembly bias effect.

Key words: cosmology: large-scale structure of Universe – galaxies: haloes – methods: statistical – methods: numerical

1 INTRODUCTION

In the Λ CDM cosmology framework, galaxies live in clumps of dark matter called dark matter halos (White & Rees 1978; Cooray & Sheth 2002). By studying the galaxy–halo connection, we can succinctly link the observed galaxy field to the dark matter density field calculated from cosmological theory (see Wechsler & Tinker 2018 for a review). One popular framework for empirically connecting galaxies to halos through a set of simple yet flexible probabilistic models is known as the Halo Occupation Distribution (HOD; e.g. Jing et al. 1998; Peacock & Smith 2000; Scoccimarro et al. 2001; White et al. 2001; Berlind & Weinberg 2002; Berlind et al. 2003; Zheng et al. 2005, 2007).

The HOD has been highly successful in describing the non-linear scale clustering of magnitude-limited galaxy samples in past galaxy redshift surveys (e.g. Zehavi et al. 2011; Parejko et al. 2013; Guo et al. 2014, 2015b; Rodríguez-Torres et al. 2016; Alam et al. 2020; Avila et al. 2020; Yuan et al. 2021b). Such HOD studies not only produce models and mocks that match the observed clustering in great detail (e.g. Smith et al. 2020; Rossi et al. 2021; Alam et al.

2021), but can reveal aspects of galaxy evolution physics (e.g. Lange et al. 2019a; Alam et al. 2020; Yuan et al. 2021a; Wang et al. 2022; Linke et al. 2022). Most recently, simulation-based forward models has employed HODs to derive cosmology constraints from non-linear scales (e.g. Lange et al. 2022; Kobayashi et al. 2022; Chapman et al. 2022; Yuan et al. 2022a; Zhai et al. 2023).

The need to understand the galaxy–halo connection is especially critical given the precision of the next generation of large-scale structure surveys, including the ongoing the Dark Energy Spectroscopic Instrument (DESI; Levi et al. 2013a; DESI Collaboration et al. 2016). DESI will obtain spectroscopic measurements of 40 million galaxies and quasars in a 14,000 deg² footprint. This represents an order-of-magnitude improvement both in the volume surveyed and the number of galaxies measured over previous surveys. DESI will achieve this by extending to significantly higher redshift, relying on a dense sample of ELGs in $0.8 < z < 1.6$. ELGs are ideal tracers because of their high density and because they exhibit a strong characteristic [O II] doublet emission line, which allows for optimal spectroscopic redshift measurements of $z = 0.5$ –2 galaxies (Drinkwater et al. 2010; Raichoor et al. 2017). For this reason, ELGs have become the premier galaxy tracers at $z > 1$ not just for DESI, but also for a slew of next-gen cosmological surveys including Prime Focus Spectrograph

* E-mail: sihany@stanford.edu

(Takada et al. 2014) and the Roman Space Telescope (Spergel et al. 2013). However, despite their importance in realizing the goals of next generation of cosmological surveys, relatively little is known about ELGs and ELG–halo connection. Moreover, ELG properties might be sensitive to redshift evolution and the details of their selection. Thus, there exists an urgent need to study their physical nature and build robust models for ELG–halo connection.

Several studies have modeled the ELG–halo connection using the relatively small eBOSS (Dawson et al. 2016) ELG sample (Favole et al. 2016; Guo et al. 2019; Avila et al. 2020). They found that the ELG clustering can be well explained by an HOD model where the central occupation peaks at approximately $10^{12}h^{-1}M_{\odot}$ halos and the satellite occupation follows a power law. More recent studies have started to find deviations from this vanilla model. Alam et al. (2020) found a small discrepancy between such vanilla HOD model and data in the ELG×LRG cross-correlations. The authors interpreted the discrepancy as potential evidence for correlated quenching, which converts some ELG satellites near LRG centrals to LRGs. Simultaneously, studies have used hydrodynamical models to investigate the ELG–halo connection. For example, Hadzhiyska et al. (2022a) found evidence for spatially correlated star formation in ELGs and a need to extend the vanilla HOD model for ELGs.

Spatial correlation in galaxy properties such as star formation rate and colors is broadly referred to as galactic conformity. The term was first coined in the context of large galaxy surveys in Weinmann et al. (2006), and the effect was confirmed observationally in numerous subsequent studies (e.g. Ann et al. 2008; Prescott et al. 2011; Wang & White 2012; Kauffmann et al. 2013; Hartley et al. 2015; Hearin et al. 2015; Knobel et al. 2015; Pahwa & Paranjape 2017; Treyer et al. 2018; Ayromlou et al. 2023). Galactic conformity is also readily produced in hydrodynamical simulations of galaxy formation (e.g. Bray et al. 2016; Rafieferantsoa & Davé 2018). However, it is not immediately clear what is driving the observed galactic conformity. While it is widely agreed on that galaxies’ dependencies on secondary halo properties other than mass, i.e. galaxy assembly bias, can produce galactic conformity, other effects that associate galaxy evolution with environmental effects can also induce galactic conformity (e.g. Paranjape et al. 2015; Zu & Mandelbaum 2018; Tinker et al. 2018).

With DESI One-Percent Data (DESI Collaboration et al. 2023b,a), we have for the first time measured ELG clustering at percent-level accuracy deep into 1-halo scales. Rocher et al. (2023) analyzed the clustering of the DESI One-Percent Survey ELG sample in an extended HOD framework. Surprisingly, the ELG auto-correlation function exhibits a large upturn at $\sim 0.1h^{-1}\text{Mpc}$ that is not readily predicted by a vanilla HOD with values calibrated on hydrodynamical simulations or eBOSS ELG HOD fits (Alam et al. 2020; Avila et al. 2020). However, the paper suggested that the small-scale amplitude can be explained by galaxy conformity, which generates excess small-separation pairs by populating ELG satellites in the same halos as ELG centrals. However, the paper also finds a degeneracy between the conformity HOD model and an extreme vanilla HOD model. A vanilla ELG HOD model can generate excess clustering on 1-halo scales by adopting a very small, even negative, satellite occupation scaling index α , which “over-load” low mass halos with ELG satellites, thus generating a large number of close ELG pairs. Rocher et al. (2023) argued qualitatively that this scenario is physically implausible, but additional arguments are needed to break the conformity- α degeneracy.

In this paper, we present a physical picture for DESI ELGs that naturally motivates the inclusion of 1-halo conformity and galaxy assembly bias in the ELG HOD model. We achieve this by combin-

ing a suite of simulated galaxy models and observations, including the auto and cross-correlation between ELGs and LRGs in the DESI One-Percent Survey. We start by presenting the DESI data sets and the clustering measurements in section 2. We use COSMOS data to put forth a physical picture of DESI ELGs in section 3. Then, we describe the HOD framework in section 4, and present evidence for ELG conformity and assembly bias in ILLUSTRISTNG in section 5. Taking inspiration from ILLUSTRISTNG, we construct extended ELG HOD models and apply them to the DESI auto and cross clustering in section 6 and 7. We further address the α -conformity degeneracy in section 8 by measuring α in ELG–cluster cross-correlation. We explore the origin of conformity in section 9 and elucidate the difference between conformity and galaxy assembly bias. In section 10, we discuss complementary works on ELG conformity and alternative theories of the origin of conformity. Finally, we conclude in section 11.

Throughout this paper, we adopt the Planck 2018 ΛCDM cosmology ($\Omega_c h^2 = 0.1200$, $\Omega_b h^2 = 0.02237$, $\sigma_8 = 0.811355$, $n_s = 0.9649$, $h = 0.6736$, $w_0 = -1$, and $w_a = 0$) (Planck Collaboration et al. 2020). We use $h^{-1}\text{Mpc}$ units for distances, $h^{-1}M_{\odot}$ for halo masses, and M_{\odot} for stellar masses.

2 DATA

The primary goal of this paper is to better understand the physical nature of the DESI ELG sample and propose motivated models to describe their clustering. In this section, we introduce the DESI One-Percent Survey, the LRG and ELG samples, and their respective auto and cross-correlation measurements.

2.1 DESI One-Percent Survey

DESI conducted its One Percent Survey as the third and final phase of its Survey Validation (SV) program in April and May of 2021. Observation fields were chosen to be in 20 non-overlapping ‘rosettes’ selected to cover major datasets from other surveys, including the Cosmic Evolution Survey (COSMOS), Hyper Suprime-Cam (HSC), Dark Energy Survey (DES) deep field, Galaxy And Mass Assembly (GAMA), Great Observatories Origins Deep Survey (GOODS), and anticipated deep fields from future Legacy Survey of Space and Time (LSST) and Euclid observations. Each rosette is observed at least 12 times, resulting in over high completeness for all targeted samples. The One-Percent survey observed approximately 90,000 LRGs, 270,000 ELGs, 30,000 QSOs, and 150,000 low-redshift galaxies known as Bright Galaxy Sample (BGS). We refer readers to DESI Collaboration et al. (2023a) and DESI Collaboration et al. (2023b) for more details. The One Percent Survey essentially produces a smaller but more complete preview version of the upcoming DESI main sample, and is ideal for calibrating galaxy–halo connection models and building high-fidelity DESI mocks.

2.2 DESI LRGs and ELGs

The Luminous Red Galaxies (LRGs) are commonly used as large-scale structure tracers due to two main advantages: 1) they are bright galaxies with the prominent 4000Å break in their spectra, thus allowing for relatively easy target selection and redshift measurements; and 2) they are highly biased tracers of the large-scale structure, thus yielding a higher S/N per-object for the BAO measurement compared to typical galaxies. The LRG target selection is defined in Zhou et al. (2020, 2023).

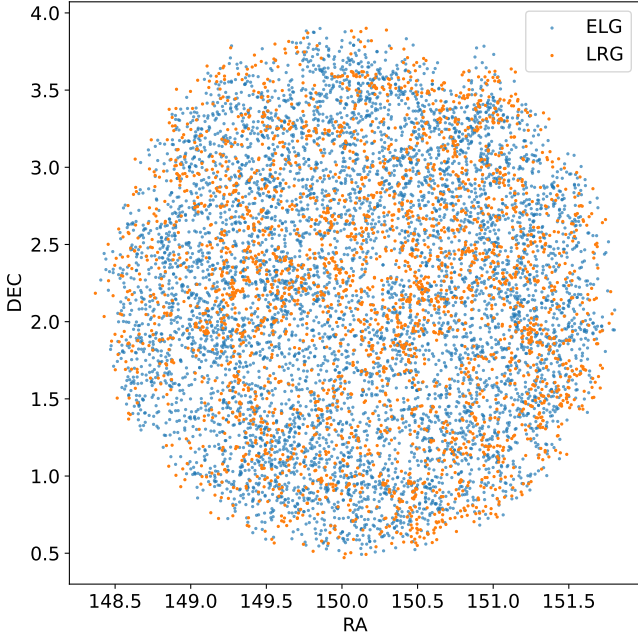


Figure 1. Scatter plot showing the projected distribution of ELGs (blue) and LRGs (orange) in $0.8 < z < 1.1$ in one of the 20 rosettes in DESI One-Percent Survey. This specific rosette also covers the COSMOS field.

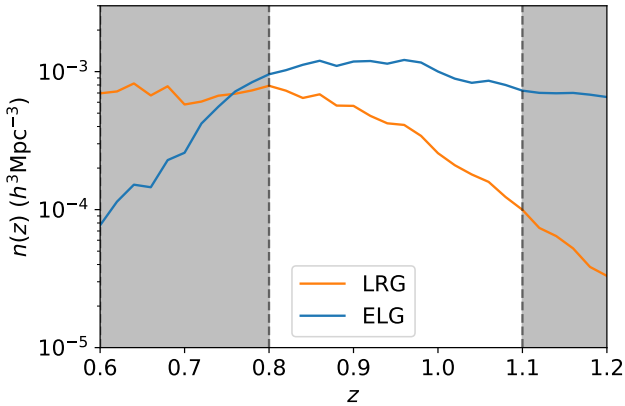


Figure 2. The mean number density of the DESI EDR LRG and ELG samples as a function of redshift. For this study, we only consider the two samples in the $0.8 < z < 1.1$ redshift regime, where the ELG sample reaches its peak number density and the LRG sample density drops off.

Emission Line Galaxies (ELG) will be the largest sample within DESI for large-scale structure studies. ELGs are bright star-forming galaxies at $z > 0.8$ and extend out to redshifts of $z < 1.6$. ELGs are particularly suited for spectroscopic surveys as they can be selected by their strong [O II] doublet emission lines, which allow for precise redshift measurements. The ELG target selection algorithm is detailed in Raichoor et al. (2020, 2023).

Figure 1 visualizes the projected distribution of DESI ELGs and LRGs in redshift range $0.8 < z < 1.1$ in one of the 20 rosettes in DESI One-Percent Survey. This rosette specifically covers the COSMOS field. We see strong spatial clustering in both samples. Figure 2 shows the mean number density of the DESI EDR LRG and ELG samples

as a function of redshift. The dashed lines denote the redshift regime we study in this analysis. Within redshift $0.8 < z < 1.1$, we obtain roughly 34,000 LRGs and 125,000 ELGs, for an average number density of $3.8 \times 10^{-4} h^3 \text{Mpc}^{-3}$ and $1.0 \times 10^{-3} h^3 \text{Mpc}^{-3}$, respectively.

2.3 Observed clustering

In this paper, we consider the projected correlation functions within and between the DESI EDR LRG and ELG samples. The construction of the EDR catalogs is described in DESI Collaboration et al. (2023b). Briefly, these LSS catalogs apply quality cuts to the data samples and provide matched random catalogs that trace the angular footprint and dN/dz of the data. Lasker (prep) describes simulations of the DESI One Percent Survey fiber assignment in order to encode via bits the fiber assignment probability of each target and thus any joint probabilities of observation for a given set of targets. We use this information to determine the pairwise-inverse-probability (Bianchi & Percival 2017) weights to use in our clustering measurements. We further apply angular up-weighting (PIP+ANG) (Percival & Bianchi 2017). Mohammad et al. (2020) showed that this weighting scheme provides an unbiased clustering down to $0.1 h^{-1} \text{Mpc}$.

The One Percent Survey LSS catalogs also include the so-called ‘FKP’ (Feldman et al. 1994) weights in order to properly weight each volume element with respect to how each sample’s number density changes with redshift,

$$w_{\text{FKP}} = 1/(1 + n(z)P_0) \quad (1)$$

where $n(z)$ is the weighted number per volume, and P_0 is a fiducial power-spectrum amplitude. For a detailed description of the weights and systematics treatment, we refer the readers to DESI Collaboration et al. (2023b).

The 2-point correlation function (2PCF) can be computed using the Landy & Szalay (1993) estimator:

$$\xi(r_p, r_\pi) = \frac{DD - 2DR + RR}{RR}, \quad (2)$$

where DD , DR , and RR are the normalized numbers of data-data, data-random, and random-random pair counts in each bin of (r_p, r_π) . r_p and r_π are transverse and line-of-sight (LoS) separations in comoving units. We can then compress the full shape $\xi(r_p, r_\pi)$ to the projected galaxy 2PCF w_p , which is the line-of-sight integral of $\xi(r_p, r_\pi)$,

$$w_p(r_p) = 2 \int_0^{r_{\pi, \text{max}}} \xi(r_p, r_\pi) dr_\pi, \quad (3)$$

We show the DESI EDR LRG and ELG auto and cross-correlations with the orange curves in Figure 3. The error bars represent 68% intervals and come from 60 jackknife regions of the One-Percent Survey footprint. The blue curves show the clustering measurement over the entire redshift range of $0.8 < z < 1.1$, whereas the orange and green curves show the clustering in the lower and higher redshift halves. We see that there is insignificant redshift evolution in the ELG auto-correlation function and the ELG×LRG cross-correlation function (see Gao et al. (2023b) for a more detailed discussion). There is more redshift evolution in the amplitude of the LRG clustering, at approximately 20% between the two lower and higher redshift halves. However, the significance of the deviation from the mean measurement in blue is rather low at only 1-2 σ . Furthermore, we measured the evolution of the LRG sample in Yuan et al. (2023), where we found a mild change of $\sim 10\%$ in the LRG linear bias in $0.8 < z < 1.1$.

In this paper, we ignore the redshift evolution of the two samples

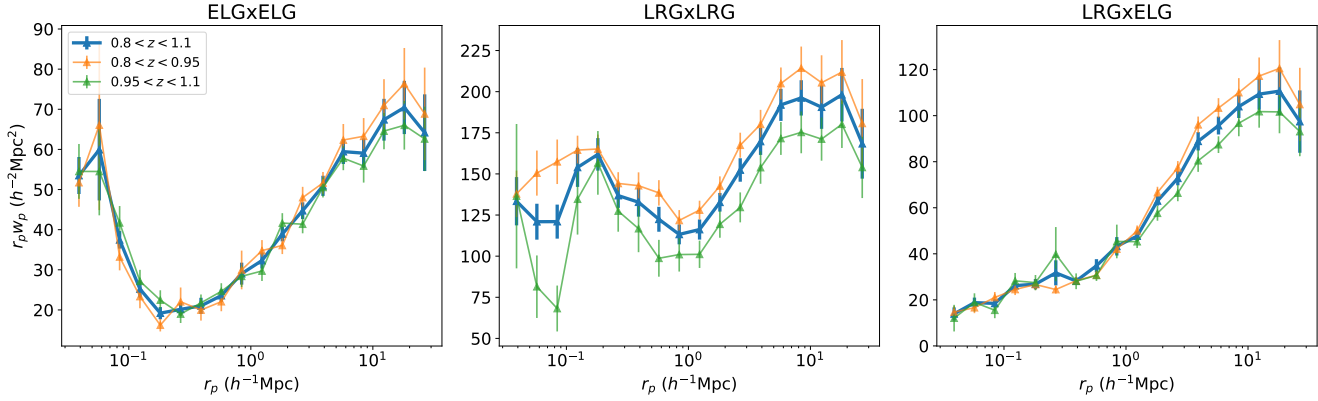


Figure 3. The projected auto and cross correlation functions of the DESI One-Percent ELG and LRG samples. The error bars on the DESI samples come from 60 jackknife regions in the survey footprint. The highlighted blue curves show the clustering in $0.8 < z < 1.1$, which we use for the following analysis. The orange and green lines show the clustering in $0.8 < z < 0.95$ and $0.95 < z < 1.1$, respectively.

and assume that the samples can be approximated with a single HOD. This is a reasonable assumption given the mild evolution. Nevertheless, we acknowledge that this is an important caveat that can impact our conclusions. We reserve a more detailed analysis of the redshift evolution of the two samples for future work.

The ELG auto-correlation function shows a dramatic upturn below $r_p < 0.2 h^{-1} \text{Mpc}$, whereas the ELG \times LRG cross-correlation shows very low amplitude at similar scales. This suggests that ELGs are highly clustered on 1-halo scales, but there are very few ELG-LRG pairs on 1-halo scales. These features were not immediately obvious in eBOSS (Avila et al. 2020; Alam et al. 2020), but have since become a focus of ELG-halo connection modeling efforts in DESI (Rocher et al. 2023; Gao et al. 2023a). The key objective of this paper is to improve our understanding of the nature of ELGs and the modeling of their clustering.

3 PROBING ELGS IN THE COSMOS FIELD

There is a relative dearth of literature exploring the nature of ELGs. In this section, we explore the nature and properties of ELGs using existing data in the COSMOS field.

COSMOS is a deep, wide area, multi-wavelength survey over 2 square degrees aimed at measuring the evolution of galaxies on scales, and is also covered in DESI EDR. The field has been observed at all accessible wavelengths from the X-ray to the radio with most of the major space-based (Hubble, Spitzer, GALEX, XMM, Chandra, Herschel, NuStar) and ground-based telescopes (Keck, Subaru, Very Large Array (VLA), European Southern Observatory Very Large Telescope (ESO-VLT), United Kingdom Infrared Telescope (UKIRT), The National Optical Astronomical Observatory (NOAO) Badde and Blanco telescopes, the Canada France Hawaii Telescope (CFHT), and others). In this section, we identify DESI ELGs in the COSMOS2020 catalogs (Weaver et al. 2022). We study the inferred galaxy properties such as stellar mass and star formation rate from existing measurements and also present a preliminary morphology analysis using Hubble Advanced Camera for Surveys (HST ACS) images.

We identify DESI ELGs in the COSMOS2020 catalog by spatially cross-matching with the DESI EDR ELG catalog in $0.8 < z < 1.1$ with an 1-arcsecond filter. Then amongst the 931 matches, we require that their best-fit photo- z be within 0.1 of the DESI redshift so that

their inferred galaxy properties are not significantly biased by their photo- z errors. We identify 929 ELG matches in COSMOS2020.

3.1 Properties from SED fits

Figure 4 presents the distribution of the inferred stellar masses and star formation rates of the ELG matches in orange, compared to all 97 thousand COSMOS galaxies in $0.8 < z < 1.1$ in blue. We also compare against the stellar mass function (SMF) of DESI ELGs inferred from $grzW1W2$ 5-band fits (green distribution; Gao et al. 2023b). The COSMOS stellar masses and star formation rates were inferred from LEPHARE (Arnouts et al. 2002; Ilbert et al. 2006), where a SED template library is fit to the observed photometry after fixing the redshift to the photo- z estimated following Laigle et al. (2016). An uncertainty of 0.2-0.3 dex is expected for the inferred masses due to systematics in the SED fitting method (Leja et al. 2019; Sorba & Sawicki 2018), and potential additional uncertainties may arise from photo- z errors.

The ELG SMF measured via COSMOS cross-matches in orange is consistent with the 5-band Legacy Survey SED fits from Gao et al. (2023b) in green above $\log_{10} M_{\text{star}}/M_{\odot} \approx 10$. This consistency is remarkable as the two SMFs come from distinct datasets and independent pipelines. The discrepancy at lower masses is possibly due to a combination of photo- z errors in the 5-band fit and other systematics in the SED fitting pipelines at lower masses. Comparing the orange SMF to the full COSMOS SMF in blue, we see that the ELGs are a mass-incomplete sample, with a peak completeness of $\approx 10\%$ at $\log_{10} M_{\text{star}}/M_{\odot} \approx 9.8$. As we show later in Section 7, this is consistent with the HOD fits, which show a peak completeness of $\sim 10\%$ in halos of $\sim 10^{12} h^{-1} M_{\odot}$.

The middle panels of Figure 4 show the distribution of ELG star formation rates relative to the full COSMOS2020 sample. Clearly, the DESI ELGs are some of the most actively star-forming galaxies. However, the peak completeness in terms of SFR is also only $\sim 10\%$ at the high SFR end, and the completeness drops off very quickly at $\log_{10} \text{SFR} < 1 M_{\odot}/\text{yr}$. A similar trend is seen in the distribution of specific star formation rate (sSFR) in the right panels, where the ELGs represent an incomplete sample of galaxies with the highest sSFRs.

To better understand ELG completeness as a function of physical properties, Figure 5 shows ELG completeness in the 2D stellar mass-SFR plane. The 2D contours show the distribution of all galaxies in

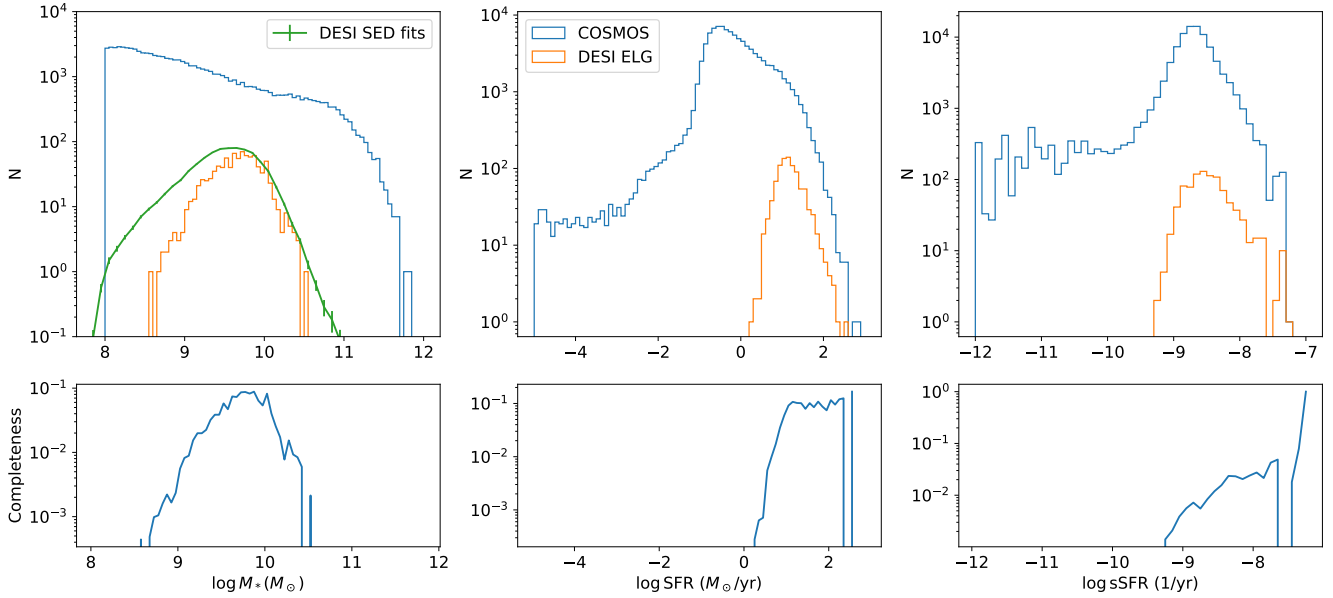


Figure 4. The distribution of stellar masses (left panel), star formation rate (middle panel), and specific star formation rate (right panel) of DESI ELGs in COSMOS field compared to all galaxies in COSMOS2020 catalog in $0.8 < z < 1.1$. In green, we also show the stellar mass function of Gao et al. (2023b) derived from fitting DESI ELG spectra. The bottom panels show the completeness of the DESI ELG sample relative to the COSMOS2020 sample.

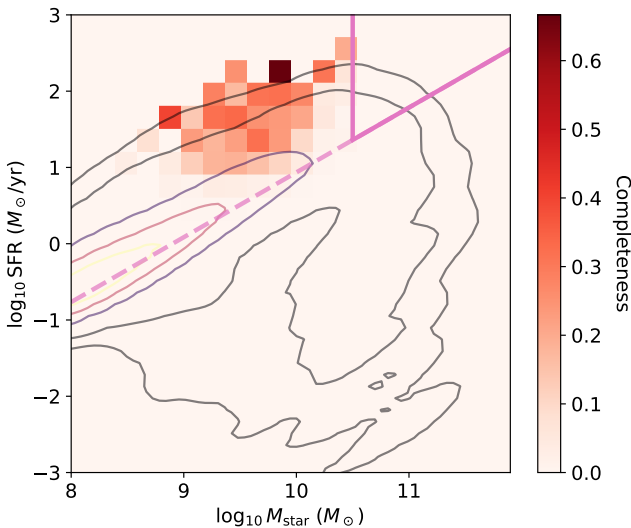


Figure 5. The completeness of ELGs relative to the underlying COSMOS galaxies in the stellar mass vs SFR plane. The contours visualize the distribution of 97k COSMOS galaxies in $0.8 < z < 1.1$. The red histograms show the completeness and distribution of ELGs. We plot the dashed line to represent the mean behavior of the star-forming main sequence. The most massive star-forming galaxies selected by the pink box are missing from the ELG sample. We compare them to DESI ELG selection cuts in Figure 6.

the COSMOS catalog. We see a star-forming main sequence (SFMS), where we have added a pink dashed line to highlight the mean trend. Note that the pink dashed line is not a fit, but simply serves as visual guide. There is also a quenched sequence to the bottom right of the plot. The completeness of the ELG population is shown with the red histograms. The ELGs are all significantly above the SFMS (by > 1 dex in most cases), populating a regime that is known as starburst

galaxies (e.g. Rodighiero et al. 2011; Schreiber et al. 2015; Elbaz et al. 2018). Several studies have found evidence that starburst galaxies are dominated by merging or interacting galaxy systems (Sanders et al. 1988; Urrutia et al. 2009; Moreno et al. 2021), thus raising the possibility that ELGs preferentially select galaxies undergoing mergers and tidal interactions with nearby galaxies. This merger hypothesis is also consistent with the fact that the ELG completeness increases with SFR. We discuss this further in Section 3.2.

In Figure 5, the peak completeness of the DESI ELG sample is approximately 65%, occurring at approximately $\log_{10} M_{\text{star}}/M_{\odot} = 9.8$ and the highest SFR end of the distribution. However, the most massive star-forming galaxies above $\log_{10} M_{\text{star}}/M_{\odot} > 10.5$ are missing from the ELG sample. To understand this incompleteness at the massive end, we select these most massive star-forming galaxies with the pink bounding box in Figure 5. We cross-match them with DESI Legacy Survey DR9 catalogs (Dey et al. 2019) to extract their photometry, and we plot their $g-r$ vs $r-z$ distribution in Figure 6. The orange and pink scatter points show the ELG sample and the high stellar mass high SFR sample, respectively. The 2D histogram shows the distribution of the full Legacy Survey sample. The black lines show the DESI ELG selection (Raichoor et al. 2023). Clearly, the most massive star-forming galaxies are rejected by the negatively sloped selection cut. Referring to Figure 3 and Figure 18 of Raichoor et al. (2023), this selection cut is chosen to optimize the fraction of ELG targets with high [O II] flux in $1.1 < z < 1.6$, which translates to high redshift success efficiency. The redder region occupied by the pink points is mostly populated with lower redshift galaxies. Thus, including this region of the color space would translate to a significantly lower redshift efficiency.

COSMOS photo- z s should be fairly accurate given that we found 929 out of the 931 ELG matches in COSMOS have photo- z errors less than 0.1. Thus, most of the galaxies selected by the pink bounding box should be indeed high redshift massive galaxies. The reason they have redder colors can be attributed to their older ages, which are inferred to be 1.5 ± 0.8 billion years compared to the ELGs' 0.6 ± 0.4 billion

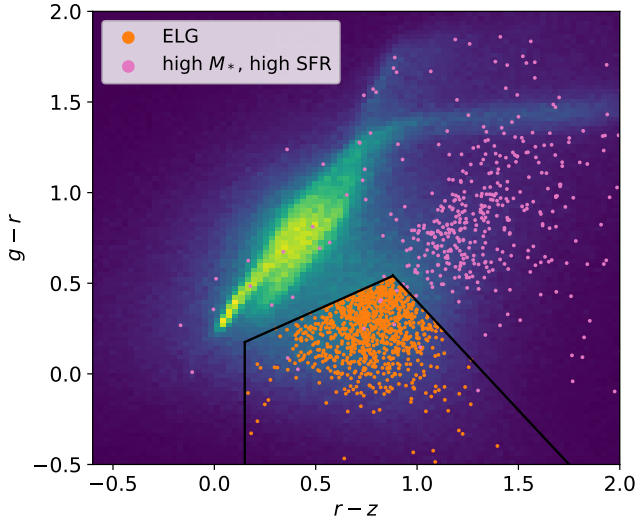


Figure 6. The $g-r$ vs $r-z$ distribution of the DESI ELGs in COSMOS compared to that of the most massive star-forming galaxies located in the region bounded by pink solid lines ($\log_{10} M_{\text{star}} > 10.5$, $\log_{10} \text{SFR} > 1.3$) in Figure 5. The 2D histogram shows the distribution of the full DESI Legacy DR9 sample. The black lines showcase the DESI EDR ELG selection cuts. Clearly, the most massive star-forming galaxies are rejected by the slanted cut with a negative slope.

years. As a result, we suggest that these galaxies are redder because of their higher metallicities and also likely dust. We conduct similar tests for galaxies that are in the same region of the stellar mass–SFR plane but are not selected as ELGs. We find these galaxies are also redder in color, likely due to dust attenuation.

It is also worth noting that the ELG sample we are considering is also at lower redshift $0.8 < z < 1.1$, outside the range that is optimized for ELG target selection. We reserve a detailed discussion of these points for a future paper. The conclusion, for now, is that while ELGs are indeed massive starburst galaxies, a significant fraction of the most massive star-forming galaxies are rejected by the ELG selection cuts in order to achieve higher redshift efficiency in $1.1 < z < 1.6$.

3.2 ELG morphology

To study ELG morphology and build more physical intuition, we can also look at Hubble images of ELGs in COSMOS. Figure 7 shows a random subset of HST ACS I-band (F814W) mosaic images of ELGs in COSMOS (Koekemoer et al. 2007; Scoville et al. 2007; Massey et al. 2009). These images have a pixel resolution of 0.03 arcsec and each image is 6 arcsec in size. For comparison, Figure 8 shows a random subset of galaxies in COSMOS that are of similar mass to DESI ELGs ($9.5 < \log_{10}(M_{\text{star}}/M_{\odot}) < 9.7$) but are not identified as ELGs. Comparing the two sets of images, it is immediately clear that ELGs are more likely to have irregular/perturbed morphologies with strong tidal features. A similar preference for irregular morphology has also been seen for star-forming galaxies in the WiggleZ survey (Drinkwater et al. 2010). Moreover, while the non-ELGs appear fairly isolated, the ELGs tend to appear in the vicinity of other irregular galaxies.

These signs of interaction may suggest that a significant fraction of ELGs are either recently merged or merging systems. This would also explain the high star formation rates of ELGs (Figures 4 and

5), since both observations and simulations have long shown that galaxy mergers can trigger star formation (e.g. Larson & Tinsley 1978; Kennicutt et al. 1987; Knapen & James 2009; Lambas et al. 2012; Ellison et al. 2013; Knapen et al. 2015; Moreno et al. 2021; Thorp et al. 2022). It is believed that such star formation stems from gas losing angular momentum and fueling centralized star formation, as a result of the non-axisymmetric structures generated by gravitational forces in an interaction (e.g. Mihos & Hernquist 1996; Hopkins et al. 2013). Though the enhancement of star formation can strongly depend on the specific configuration of the merger, orbital parameters, mass ratios, local densities, and gas contents of the disks (e.g. Cox et al. 2008; Lin et al. 2010; Davies et al. 2015; Moreno et al. 2015; Fensch et al. 2017), at least some mergers can also trigger short periods of extreme star formation, known as starbursts, due to tidal interactions compressing and shocking the gas (e.g. Barnes 2004; Kim et al. 2009; Saitoh et al. 2009; Cortijo-Ferrero et al. 2017; Verrico et al. 2023). Thus, our picture of merger-triggered star formation in ELGs is solidly grounded in our existing understanding of galaxy evolution.

We further substantiate our argument by cross-matching the ELG sample with other galaxy catalogs in the COSMOS field. We first consider the MORPHEUS catalog (Hausen & Robertson 2020), which uses a deep learning-based model to generate morphology classifications for galaxies on HST data in the CANDLES field. We found 20 matches within our ELG sample in $0.8 < z < 1.1$ and 89 non-ELG matches with stellar mass $9.5 < \log_{10}(M_{\text{star}}/M_{\odot}) < 9.7$ for comparison. For each galaxy, the MORPHEUS catalog assigns probabilities (summing to unity) of having spheroid, disk, or irregular morphologies. We showcase the mean classification probabilities of ELGs and non-ELGs in Figure 9. Compared to non-ELGs, the ELGs are more likely to be classified as irregular and less likely to be classified as disks, again suggesting that ELGs tend to be more disturbed than non-ELGs.

To compare the merger rate in ELGs versus non-ELGs in a more quantitative way, we cross-match with the late-stage merger catalog compiled by Lackner et al. (2014). This catalog aimed to select galaxy mergers in their final stages before coalescence (i.e., when the galaxy nuclei are intact but at very small \sim kpc separations) by using a high-pass filter to identify multiple peaks in the surface brightness profiles of COSMOS HST ACS images. We cross-match the ELG sample against this merger catalog and find that $(9.8 \pm 1.0)\%$ of ELGs are identified as late-stage mergers. Of a control sample of non-ELGs (in a similar mass and redshift range as the ELG sample), only $(0.97 \pm 0.32)\%$ are late-stage mergers. The errors reported here are standard deviations estimated by randomly drawing 10^4 bootstrap subsamples from the ELG and non-ELG samples.

Importantly, the Lackner et al. (2014) catalog is incomplete in several ways: it is based on a source sample that is less complete than the COSMOS2020 catalog from which we draw our ELG sample, it only considers a narrow definition of “late-stage” mergers, and it may also miss up to 80% of late-stage mergers at $z > 0.5$ (Appendix A of Lackner et al. 2014). As a result, the percentages of ELGs and non-ELGs in this catalog do not translate to absolute merger rates. However, the relative difference between the two classes—that ELGs are 10 times more likely to be identified as late-stage mergers than non-ELGs—further supports our argument that a significant fraction of ELGs are mergers.

The physical nature of the mergers in ELGs remains unclear. Returning to the cutouts in Figure 7, we see that the disk ELGs are accompanied by nearby galaxies that are in the process of merging or feeding the ELGs with tidal tails. We speculate that there are potentially multiple star formation triggers in ELGs depending on

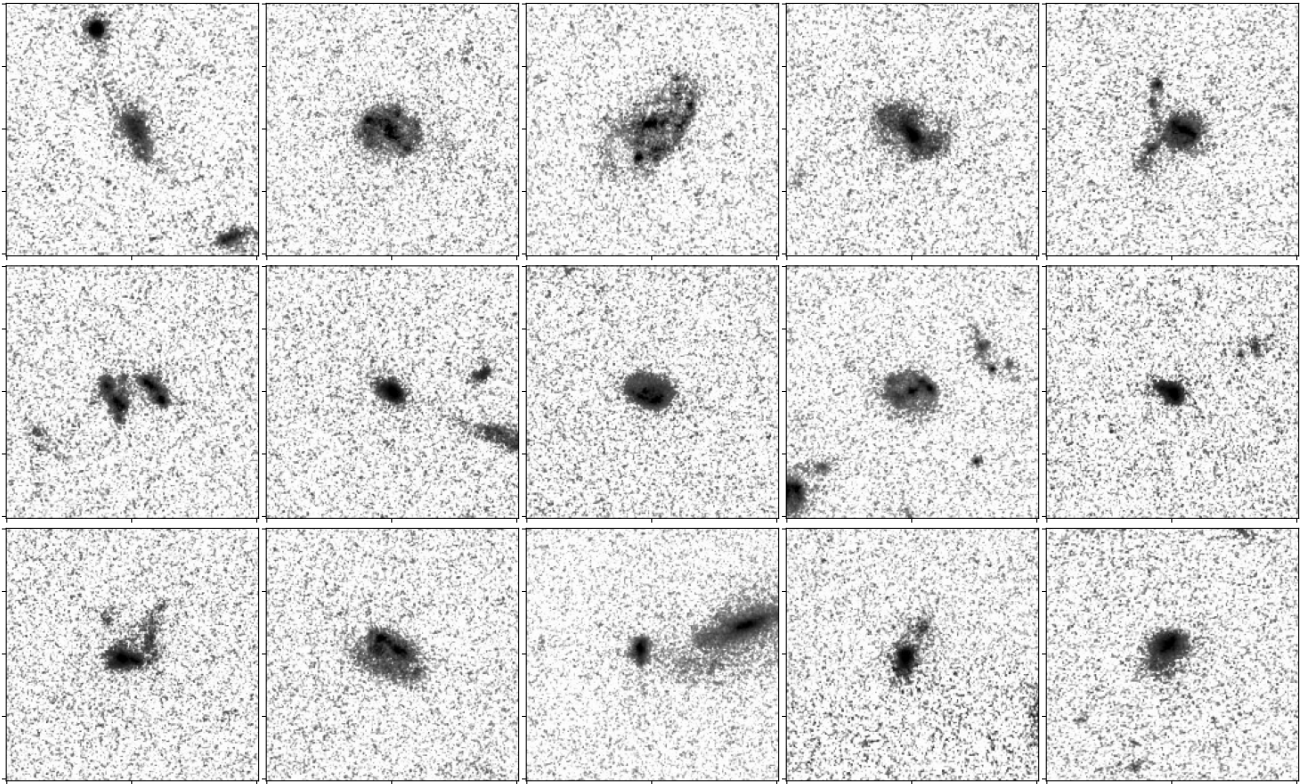


Figure 7. HST ACS (F814W) images of DESI ELGs in COSMOS. Each image stamp is 6 arcsec per side. Compared to Figure 8, which shows galaxies of similar mass that are not identified as ELGs, ELGs show significantly more irregular morphology. ELGs also tend to appear as recently merged or part of soon-to-be-merged systems. This is consistent with our hypothesis that ELGs exhibit star formation triggered by tidal interactions.

the environment and the mass ratio. The disk ELGs may be more dynamically stable, getting their star formation via gas accretion. In contrast, the irregular ELGs could be undergoing major or minor mergers that trigger starbursts via tidal compression. Further studies are needed to test this hypothesis.

The merger-triggered starburst scenario naturally produces to 1-halo conformity in the ELG population. Given reservoirs of molecular gas, the tidal interactions induced by mergers can ignite star formation on both sides of the merger. As a result, ELG satellites would tend to appear in close pairs with ELG centrals, boosting the clustering on small scales. This type of conformity is also distinct from galaxy assembly bias as it is not directly tied to dark matter assembly, but is simply a result of proximity to neighbour galaxies and neighbour galaxy types.

4 HOD MODELING

A key objective of this paper is to explore ELG–halo connection models that describe the observed ELG clustering in detail. The Halo Occupation Distribution (HOD) is a simple yet powerful theoretical framework for predicting and interpreting galaxy clustering on non-linear scales. In this section, we review the basics of the HOD framework, motivate the need for extensions beyond the vanilla HOD model, and present definitions of conformity and galaxy assembly bias as plausible model extensions for ELGs.

4.1 Vanilla HOD

The HOD model relates galaxies to their dark matter halo counterparts via a concise statistical relationship. In its simplest (vanilla) form, the HOD is summarized by $P(N|M)$, i.e. the probability of hosting N galaxies given a halo of mass M . In the assumption of halo mass being the only relevant quantity, the HOD is a complete model of galaxy occupation. Historically, Kravtsov et al. (2004) was amongst the first to show that the HOD can accurately predict the clustering of galaxy-size subhalos down to $\sim 100h^{-1}\text{Mpc}$ in a dark matter only N-body simulation. Then a series of studies demonstrated that a simple HOD model can describe the clustering of luminosity-limited galaxy samples at a variety of redshifts (e.g. Zehavi et al. 2005; Conroy et al. 2006; Zehavi et al. 2011). At the same time, the same HOD framework was shown to also describe the clustering of color-magnitude selected LRG samples (e.g. Zheng et al. 2009; Watson et al. 2010; Parejko et al. 2013; Rodríguez-Torres et al. 2016). Zheng et al. (2007) and Coil et al. (2008) further demonstrated the validity of HOD modeling up to $z \sim 1$.

LRGs are selected to have high completeness at the massive end, and their clustering has been shown to be well described by the following model (e.g. Zheng et al. 2005, 2007; Kwan et al. 2015; Yuan et al. 2021b):

$$\bar{n}_{\text{cent}}^{\text{LRG}}(M) = \frac{f_{\text{ic}}}{2} \operatorname{erfc} \left[\frac{\log_{10}(M_{\text{cut}}/M)}{\sqrt{2}\sigma} \right], \quad (4)$$

$$\bar{n}_{\text{sat}}^{\text{LRG}}(M) = \left[\frac{M - \kappa M_{\text{cut}}}{M_1} \right]^{\alpha} \bar{n}_{\text{cent}}^{\text{LRG}}(M). \quad (5)$$

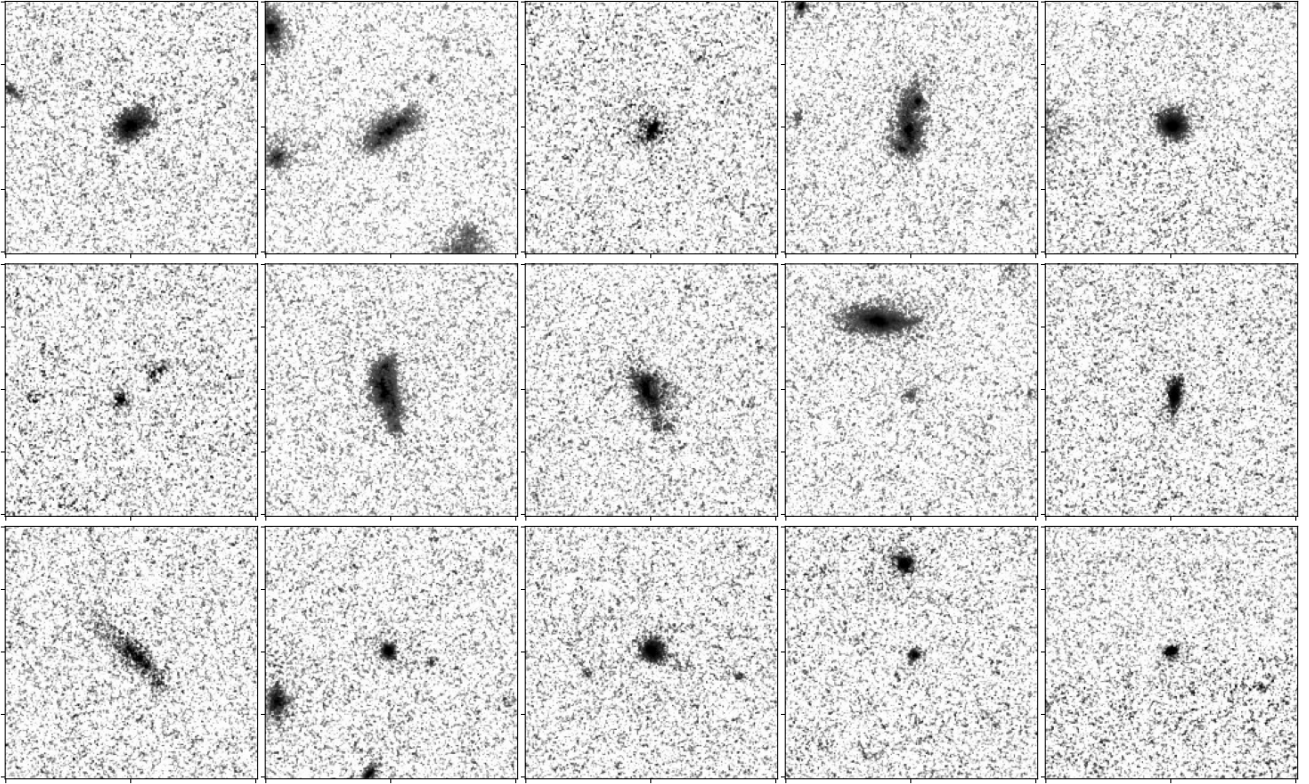


Figure 8. HST ACS (F814W) images of galaxies in COSMOS that are not identified as DESI ELGs but are of similar masses ($9.5 < \log_{10}(M_{\text{star}}/M_{\odot}) < 9.7$). Each image stamp is a 6 arcsec per side. Compared to the ELGs in Figure 7, these galaxies tend to be more nuclear and less perturbed.

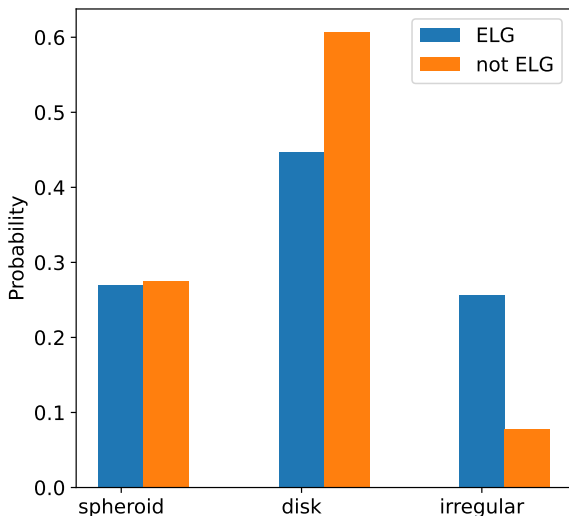


Figure 9. The mean morphology probability of ELGs and non-ELGs at similar masses classified by the MORPHEUS model using available HST images. The ELGs are more likely to be classified as irregular than non-ELGs at similar masses.

In this model, M_{cut} characterizes the minimum halo mass to host a central galaxy. M_1 characterizes the typical halo mass that hosts one satellite galaxy. σ describes the steepness of the transition from 0 to 1 in the number of central galaxies. α is the power law index on the number of satellite galaxies. κM_{cut} gives the minimum halo mass to

host a satellite galaxy. We have added a modulation term $\bar{n}_{\text{cent}}^{\text{LRG}}(M)$ to the satellite occupation function to avoid scenarios where LRG satellites occupy halos not massive enough to host LRG centrals. We have also included an incompleteness parameter f_{ic} , which is a downsampling factor controlling the overall number density of the mock galaxies. This parameter is relevant when trying to match the observed mean density of the galaxies in addition to clustering measurements. By definition, $0 < f_{\text{ic}} \leq 1$.

ELGs are selected based on [O II] luminosity, which should trace star formation, and are known to have a rather low characteristic halo mass. Distinct HOD analytic forms have been developed for ELGs, and it was found that central models that show a peaked distribution with small to no contribution from the massive end tend to describe the observed clustering well (Alam et al. 2020; Avila et al. 2020). For this paper, we adopt the mHMQ model from Rocher et al. (2023) as the vanilla model. This is a slightly modified version of the HMQ model presented in Alam et al. (2020). Here we use a notation that is consistent with Yuan et al. (2022b) but slightly different than Rocher et al. (2023). The two notations are completely equivalent.

In the vanilla model, the number of ELG centrals is given by

$$\bar{n}_{\text{cent}}^{\text{ELG}}(M) = p_{\text{max}} \phi(M) \Phi(\gamma M), \quad (6)$$

where,

$$\phi(x) = \mathcal{N}(\log_{10} M_{\text{cut}}, \sigma_M) \quad (7)$$

$$\Phi(x) = 2 \int_{-\infty}^x \phi(t) dt = 1 + \text{erf}\left(\frac{x}{\sqrt{2}}\right). \quad (8)$$

We refer to Alam et al. (2020) for detailed descriptions of each

parameter. Briefly, p_{\max} controls the peak completeness in the central occupation. $\phi(M)$ defines Gaussian distribution with peak position determined by M_{cut} and width determined by σ_M . $\Phi(\gamma M)$ introduces asymmetry to the Gaussian with a tilt parameter γ .

For the satellite galaxies, we adopt a power law model,

$$\bar{n}_{\text{sat}}^{\text{ELG}}(M) = \left[\frac{M - \kappa M_{\text{cut}}}{M_1} \right]^\alpha, \quad (9)$$

where the parameters carry similar meanings as the LRG satellite case. Note that we do not modulate with n_{cent} because ELG selection is driven by bursty star formation, so we want to allow for the possibility of ELG satellites existing in halos less massive than those hosting ELG centrals.

In the vanilla HOD models, the position and velocity of the central galaxy are set to be the same as those the halo center, specifically the L2 subhalo center-of-mass for the COMPASO halos. For the satellite galaxies, they are randomly assigned to halo particles with uniform weights, each satellite inheriting the position and velocity of its host particle. We defer the readers to Yuan et al. (2021b) for implementation details.

4.2 Conformity and galaxy assembly bias

Rocher et al. (2023) showed that the vanilla HOD struggles to describe the ELG auto-correlation function observed in DESI at small scales, and that extensions to the vanilla HOD models are needed. Recent studies using simulated galaxy models have identified galaxy assembly bias and galaxy conformity as secondary effects that are both well motivated and can potentially explain the observed clustering (e.g. Contreras et al. 2023; Hadzhiyska et al. 2022a; Wang et al. 2022; Beltz-Mohrmann et al. 2023; Yuan et al. 2021a). In this subsection, we introduce these two effects and offer succinct definitions in the context of this paper.

Galaxy assembly bias is defined as follows: At fixed halo mass, the galaxy properties or number of galaxies within dark matter halos may depend on secondary halo properties. In an HOD, this is expressed as $P(N|M, x)$, where x is some secondary halo property beyond halo mass that is correlated with the assembly history of the halo (Wechsler & Tinker 2018). Galaxy assembly bias is relevant for galaxy clustering analyses because halo clustering depends on halo assembly history (an effect known as halo assembly bias). Thus, galaxy assembly bias would lead to a signature in galaxy clustering as well (e.g. Gao et al. 2005; Zentner et al. 2005; Wechsler et al. 2006; Gao & White 2007; Croton et al. 2007; Li et al. 2008; Miyatake et al. 2016). There is an extensive literature studying galaxy assembly bias in simulations and data in the last decades (e.g. Zhu et al. 2006; Zentner et al. 2014; Pujol & Gaztañaga 2014; Hearin et al. 2016a; Artale et al. 2018; Zehavi et al. 2018; Bose et al. 2019; Yuan et al. 2021a; Lange et al. 2019b; Contreras et al. 2019; Xu et al. 2021a; Wang et al. 2022; Salcedo et al. 2022; Beltz-Mohrmann et al. 2023). For a review of this topic, we refer the reader to Wechsler & Tinker (2018).

In this paper, **Conformity** refers to the phenomenon where the properties or number of satellites depends on the property of the central galaxy. In an HOD, conformity can be expressed as $P(N_{\text{satellite}}|M, x_{\text{central}})$, where x_{central} is some property of the central galaxy, such as galaxy type or color. The conformity definition is considerably more strict than historical notions of galactic conformity, which generically refers to some level of spatial correlation in galaxy properties (e.g. Weinmann et al. 2006; Kauffmann et al. 2013; Hearin et al. 2015). Our definition specifically refers to a 1-halo central-satellite conformity, as opposed to 2-halo conformity where

the properties of galaxies in adjacent halos might be correlated, or a 1-halo satellite-satellite conformity where the properties of satellites in the same halo might be mutually dependent. Discussion of these other types of conformity are interesting but beyond the scope of this paper.

Conformity in certain forms have been regarded as an emergent phenomenon of halo and galaxy assembly bias (e.g. Hearin et al. 2015, 2016b; Berti et al. 2017). Specifically, Hearin et al. (2016b) argued that 2-halo conformity is a direct result of correlated halo accretion rate, which arises because neighboring halos are subject to the same large-scale tidal field. Strong tidal effects inhibit mass accretion into halos, resulting in spatially correlation star formation. The same paper argued that 1-halo conformity can be a result of 2-halo conformity at higher redshift. If halo accretion is the sole origin of conformity at fixed halo mass, then conformity is simply an alternative quantification of galaxy assembly bias.

However, a key point of this paper is to show that the 1-halo conformity we find is not necessarily degenerate with galaxy/halo assembly bias. In our definition, $P(N_{\text{satellite}}|M, x_{\text{central}})$, conformity is only degenerate with galaxy assembly bias if the relevant central property x_{central} is fully determined by the dark matter assembly of the host halo. In fact, as we show in section 3, section 5, and section 10, the conformity we see in DESI ELGs is likely a result of merger-driven starburst, which is not a direct result of halo accretion. This type of conformity is separate from galaxy assembly bias.

We present our implementations of galaxy assembly bias and conformity in section 6.

5 CONFORMITY AND ASSEMBLY BIAS IN ILLUSTRISTNG

We first seek evidence for conformity and galaxy assembly bias and test their effects on clustering in the publicly available ILLUSTRISTNG hydrodynamical simulation. Hydrodynamical simulations are valuable because they self-consistently model galaxy evolution through detailed recipes of stellar evolution, various feedback process, magnetic fields, and etc. They allow us to statistically study galaxy evolution in a physically plausible setting. They are particularly well suited for probing gaps in our galaxy evolution theory and building up more sophisticated models.

5.1 ILLUSTRISTNG

ILLUSTRISTNG is a state-of-the-art magneto-hydrodynamic simulation suite (Pillepich et al. 2018; Marinacci et al. 2018; Naiman et al. 2018; Springel et al. 2018; Nelson et al. 2019a, 2018; Pillepich et al. 2019; Nelson et al. 2019b). ILLUSTRISTNG were carried out using the AREPO code (Springel 2010) with cosmological parameters consistent with the *Planck 2015* analysis (Planck Collaboration et al. 2016). These simulations feature a series of improvements compared with their predecessor, ILLUSTRIS, such as improved kinetic AGN feedback and galactic wind models, as well as the inclusion of magnetic fields.

In particular, we utilize the ILLUSTRISTNG-300-1 box, the largest high-resolution hydrodynamical simulation from the suite. The size of its periodic box is $205h^{-1}\text{Mpc}$ with 2500^3 DM particles and 2500^3 gas cells, implying a DM particle mass of $3.98 \times 10^7 h^{-1}M_{\odot}$ and baryonic mass of $7.44 \times 10^6 h^{-1}M_{\odot}$. We also use the dark-matter-only (DMO) counterpart of the ILLUSTRISTNG-300-1 box, ILLUSTRISTNG-300-Dark, which was evolved with the same initial conditions and the same number of dark matter particles (2500^3), each with particle mass of $4.73 \times 10^7 h^{-1}M_{\odot}$.

The haloes (groups) in ILLUSTRISTNG-300-Dark are found with a standard friends-of-friends (FoF) algorithm with linking length $b = 0.2$ (in units of the mean inter-particle spacing) run on the dark matter particles, while the subhaloes are identified using the SUBFIND algorithm (Springel et al. 2001), which detects substructure within the groups and defines locally overdense, self-bound particle groups. For this paper, we analyse the simulations at redshift $z = 0.8$.

5.2 Mock sample selection

To select DESI-like galaxies, we first calculate DESI-like photometry for all ILLUSTRISTNG galaxies. The technical details are described in Yuan et al. (2022b) and Hadzhiyska et al. (2021). Essentially, we use the Flexible Stellar Population Synthesis code to calculate raw galaxy fluxes in each DESI photometric bands (FSPS, Conroy & Gunn 2010). Then we obtain the final DESI magnitudes by feeding the raw fluxes through an empirical model of dust attenuation, where the model parameters are roughly calibrated on recent observational measurements. Finally, we apply DESI color-magnitude cuts to obtain mock LRG and ELG samples (Zhou et al. 2020, 2023; Raichoor et al. 2020, 2023). We select 4608 LRGs, corresponding to a density of approximately $5 \times 10^{-4} h^3 \text{Mpc}^{-3}$; and 8637 ELGs, corresponding to a density of roughly $1 \times 10^{-3} h^3 \text{Mpc}^{-3}$.

5.3 Galaxy assembly bias tests

There have been a series of studies that have characterized the effect of galaxy assembly bias in ILLUSTRISTNG. We summarize those results here.

For LRGs, the predominant signal is a correlation with a secondary property that connects to local overdensity on scales of a few megaparsecs. Yuan et al. (2022b) and Hadzhiyska et al. (2020) found that HODs parameterized on halo mass and local environment are able to recover the LRG clustering seen in ILLUSTRISTNG LRG samples, and ignoring the secondary dependency can result in a significant bias in clustering prediction between 10% and 20%. Delgado et al. (2022) compared different secondary halo properties and found the local environment to be the best tracer of secondary biases. More recently, Hadzhiyska et al. (2022a) confirmed these results using the larger MILLENIUMTNG simulations (MTNG; Hernández-Aguayo et al. 2022; Bose et al. 2022; Pakmor et al. 2022), while Xu et al. (2021b) found similar trends in semi-analytic galaxy mocks. Yuan et al. (2021a) found the BOSS CMASS LRG sample to also favor the inclusion of an environment-based galaxy assembly bias model.

For ELGs, the galaxy assembly bias signal is much less certain, especially given the limited volume of ILLUSTRISTNG. Hadzhiyska et al. (2021) found a $\sim 4\%$ bias in clustering prediction when ignoring any secondary bias, compared to the 10-20% for LRGs. With MTNG, Hadzhiyska et al. (2022a) found a similar but statistically significant signal of 5-10% bias in the $z = 1$ ELG clustering. Hadzhiyska et al. (2022a) compared different secondary halo properties and found that the local shear calculated on scales of approximately $1 h^{-1} \text{Mpc}$ to be the best tracer of ELG assembly bias. Beyond hydrodynamical simulations, Jiménez et al. (2021) found scale-dependent ELG assembly bias signature in a semi-analytic model approach.

5.4 Conformity tests

In this section, we probe for central-satellite conformity in mock LRG and ELG samples in ILLUSTRISTNG. First of all, conformity is irrelevant for LRG satellites as all LRG satellites living in high mass

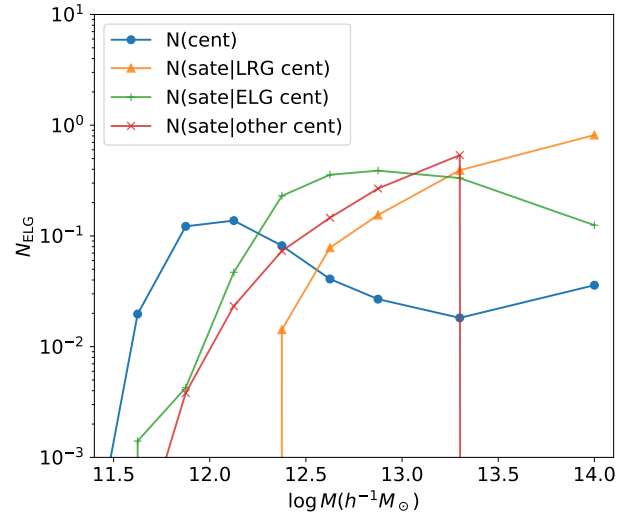


Figure 10. The mean HOD of the ILLUSTRISTNG ELG sample. We break the satellite occupation distribution into three conditional probabilities. The green curve shows the mean number of ELG satellites when the halo also hosts an ELG central. The orange curve shows the number of ELG satellites when the halo hosts an LRG central. The red curve shows the case when the central is neither an ELG or LRG. We see clear signatures of conformity.

halos that are essentially guaranteed to host LRG centrals. Thus, conformity is only relevant for modeling the occupation of ELG satellites.

Figure 10 shows the ELG HOD as measured in the ILLUSTRISTNG sample. The blue line shows the occupation of the ELG centrals. The satellite occupation is broken into three scenarios: satellites around and ELG central in green; satellites around LRG central in orange; and satellites around centrals that are neither in red. There is clear indication of conformity: at fixed halo mass, the number of satellites is largest when the central is an ELG, and lowest when the central is an LRG. At the largest halo mass, the green line unexpectedly drops below the orange line, but we suspect it is simply because of low signal-to-noise due to the limited sample size at high masses. We also expect ELG centrals to be quite rare at the high mass end and that they should not contribute significantly to the clustering.

Yuan et al. (2022b) showed that the vanilla HOD for ILLUSTRISTNG ELGs can be well described by a skewed Gaussian model for centrals and a power law model for the satellites (See Equation 9-13 of said paper and also Alam et al. (2020)). Judging by Figure 10, a simple approach to modeling satellite-central conformity is simply by scaling the satellite occupation as a function of the central galaxy type. We will construct such models and test them against DESI data in section 6-7.

To test how conformity affects clustering, we conduct several shuffling tests similar to those used in Yuan et al. (2022b); Hadzhiyska et al. (2020). Specifically, we shuffle the galaxy contents amongst halos of the same mass and compare the clustering of galaxy sample before and after the shuffling. This shuffling procedure removes any secondary dependency of the galaxy-halo connection one anything other than halo mass—such as a dependency on galaxy type of nearby galaxies, as predicted by conformity. Thus any change in the clustering due to shuffling would indicate the effect of one or more secondary dependencies on galaxy clustering.

Figure 11 showcases the projected auto and cross-correlations of the ILLUSTRISTNG LRG and ELG mock samples before shuffling in

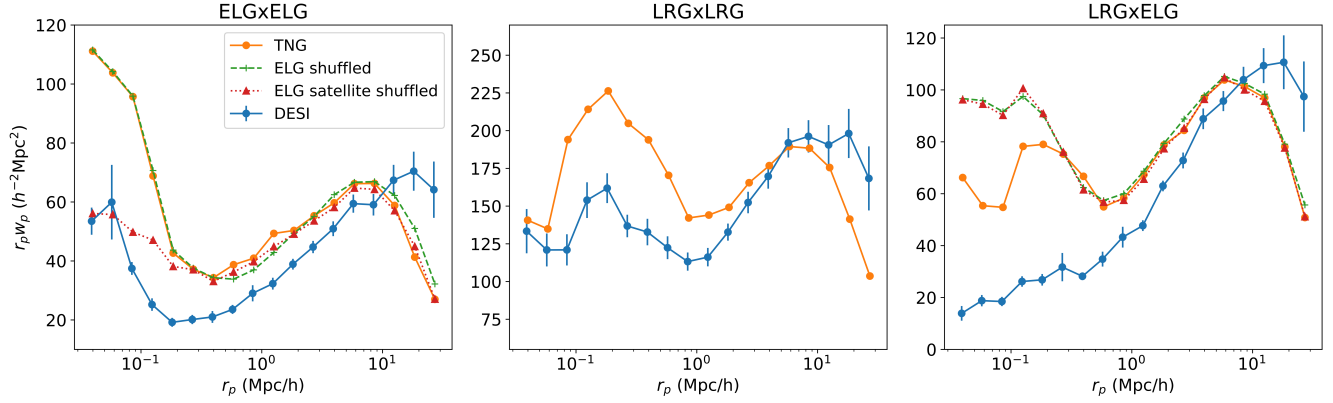


Figure 11. The clustering of mock LRG and ELG samples selected in ILLUSTRISTNG (orange), and the effects when two different shuffling routines are applied to the ELG sample in ILLUSTRISTNG (green and red). Green curves shuffle both the ELG central and satellites to test for 2-halo conformity and galaxy assembly bias, whereas the red curves shuffle just the ELG satellites while holding the centrals fixed. The left panel shows a significant decrease in small-scale amplitude when only the ELG satellites are shuffled, suggesting ELG satellites preferentially occupy halos with ELG centrals. The right panel shows the small-scale amplitude increasing when the ELGs are shuffled, suggesting that ELG satellites preferentially occupy halos without LRG centrals. The changes in clustering on very small scales suggest strong 1-halo conformity in the ELG sample. The fact that shuffling does not alter clustering on $\sim 10h^{-1}$ Mpc scales suggests the lack of 2-halo conformity.

orange and post shuffling in green and red. We also show the DESI auto and cross correlation measurements in blue for comparison. We approximate the error bars on the ILLUSTRISTNG samples as simply the DESI jackknife errors re-scaled by the ILLUSTRISTNG sample size. We see that the amplitude of the mock clustering roughly agrees with the DESI One-Percent data, and the shape of the mock auto-correlations produce the right qualitative features. This suggests that our LRG and ELG mock samples are reasonable approximations of the corresponding DESI samples. ILLUSTRISTNG ELGs also produce a similar upturn at small separation in the auto-correlation function. However, there is a large deviation in the cross-correlation measurement, where the DESI measurement shows a much stronger anti-correlation between the ELG and LRG samples. This could be due to insufficient quenching of blue galaxies near red galaxies in ILLUSTRISTNG, or due to systematics in the modeling of dust attenuation and sample selection.

The green dashed curves in Figure 11 show the clustering of the sample after shuffling ELGs amongst halos of the same mass. Specifically, we take all ELGs (both centrals and satellites) in a halo, and randomly assign them to another halo of the same mass, while preserving the relative positions of the ELGs within the same halo, and we repeat this process for all halos. This test serves to check for any indications of galaxy assembly bias or 2-halo conformity in the ELG sample. The red dotted curves show the clustering of the sample after shuffling only the ELG satellites amongst halos of the same mass. Shuffling only the satellites while holding the centrals in place disrupts any 1-halo central-satellite conformity that might exist. Thus, any changes in the clustering as a result suggests that the central and satellite occupations are not independent and the existence of 1-halo conformity.

On the left hand panel, the dashed green curve agrees perfectly with the unshuffled sample shown in orange. This suggests that the mock ELG sample does not show significant net effect of galaxy assembly bias and 2-halo conformity at the precision available with ILLUSTRISTNG. While this is contradictory to the evidence for ELG assembly bias found in MTNG and semi-analytic models, we are likely limited by the small volume of ILLUSTRISTNG. We continue to search for evidence of ELG assembly bias in DESI data in section 7. However, the dotted red curve shows that the satellite shuffling sig-

nificantly reduces the amplitude of ELG auto-correlation function on 1-halo scales. This suggests a strong positive conformity between ELG centrals and satellites in ILLUSTRISTNG. The fact that this effect only shows up when shuffling satellites but not when shuffling both centrals and satellites together demonstrates that the 1-halo conformity is independent from assembly bias. The observed DESI ELG auto-correlation also shows a large 1-halo upturn similar to the ILLUSTRISTNG ELGs, suggesting that a strong ELG conformity signature might also exist in the DESI ELG sample. We will test this claim in section 8-7.

On the LRG×ELG panel on the right panel of Figure 11, the green dashed line is also consistent with the orange line on scales beyond $r_p \sim 1h^{-1}$ Mpc. However, on smaller scales, the shuffled sample shows a larger clustering amplitude than the unshuffled sample. The satellite shuffling also shows an identical effect as shuffling the full ELG sample. This suggests a negative 1-halo conformity between LRGs and ELGs, specifically, ELG satellites disfavor halos with LRG centrals. This fits our picture of ELGs as merger-driven starbursts, as LRG centrals are biased tracers and tend to live in denser environments than ELGs. In denser environments, merger rates are low due to tidal stripping, and the mergers that do happen in dense environments tend to be “dry” (meaning no molecular gas) and thus do not trigger (or even suppress) star formation (Tran et al. 2008; Lin et al. 2010; Hester & Tasitsiomi 2010).

Comparing the LRG×ELG cross-correlations in ILLUSTRISTNG with DESI in blue shows that the two samples might be significantly more anti-correlated in data, suggesting that massive red centrals may turn off nearby star formation much more effectively than we thought. To illustrate this point more, the dashed curve in Figure 12 shows the cross-correlation measurement in ILLUSTRISTNG when we remove all ELG satellites in halos with LRG centrals. The fact that the DESI measurement lies in between the two orange lines on small scales suggests that while there are still ELG satellites around LRG centrals in data, the data display stronger anti-conformity between ELG satellites and LRG centrals than predicted by ILLUSTRISTNG.

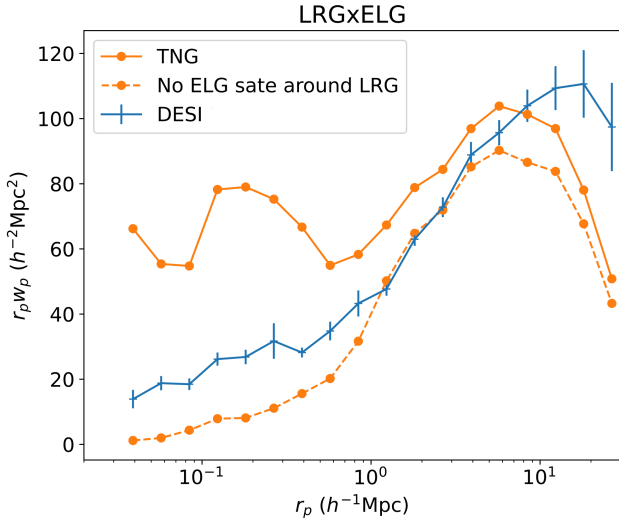


Figure 12. The effect of removing all ELG satellites with LRG centrals on the projected LRG \times ELG cross-correlation function. The solid orange line shows the clustering of the ILLUSTRISTNG ELG sample, and the dashed orange line shows the clustering of the same sample but removing all ELG satellites that are in halos with LRG centrals. The dashed orange line shares a similar shape as the observed DESI cross-correlation, albeit with even low clustering amplitude on 1-halo scales. This suggests that the ELG and LRG sample in DESI are likely more anti-correlated than seen in ILLUSTRISTNG.

6 DESI HOD ANALYSIS FRAMEWORK

Given the evidence for conformity and galaxy assembly bias in ILLUSTRISTNG, we now model these effects in a multi-tracer HOD framework and test the model against DESI auto- and cross-correlation data. We first describe the model and methodology of the HOD analysis in this section, and then we present the results in the next section.

6.1 ABACUSUMMIT simulations

To model the underlying dark matter density field, we use the ABACUSUMMIT simulation suite, which is a set of large, high-accuracy cosmological N-body simulations using the ABACUS N-body code (Maksimova et al. 2021; Garrison et al. 2019, 2021). This suite is designed to meet the Cosmological Simulation Requirements of the Dark Energy Spectroscopic Instrument (DESI) survey (Levi et al. 2013b). For this analysis, we use the $z = 0.8$ snapshot of the AbacusSummit_base_c000_ph000 box, which contains 6912^3 particles within a $(2h^{-1}\text{Gpc})^3$ volume, yielding a particle mass of $2.1 \times 10^9 h^{-1} M_\odot$. The simulations relevant for this analysis assumes Planck 2018 cosmology.¹

The ABACUSUMMIT also uses the COMPASO halo finder, which is a highly efficient on-the-fly group finder (Hadzhiyska et al. 2022b). COMPASO builds on the existing spherical overdensity (SO) algorithm by taking into consideration the tidal radius around a smaller halo before competitively assigning halo membership to the particles in an effort to more effectively deblend halos.

¹ For more details, see <https://abacussummit.readthedocs.io/en/latest/abacussummit.html>

6.2 ABACUSHOD

We use the highly optimised ABACUSHOD package to forward model galaxy mocks and compute galaxy clustering (Yuan et al. 2021b). The code is highly efficient and is specifically designed for repeated HOD evaluations on ABACUSUMMIT boxes. The package enables multi-tracer galaxy assignment and incorporates a range of physically motivated HOD extensions, such as conformity and assembly bias. The code is publicly available as a part of the ABACUSUTILS package at <https://github.com/abacusorg/abacusutils>. Example usage can be found at <https://abacusutils.readthedocs.io/en/latest/hod.html>.

We described the vanilla mass-only HOD models in section 4. Here we describe introduce extensions that model effects of galaxy assembly bias and conformity. To include assembly bias into the HOD model, we follow the ABACUSHOD implementation where $\log_{10} M_{\text{cut}}$ and $\log_{10} M_1$ are modified through the following parameterization:

$$\log_{10} M_{\text{cut}}^{\text{mod}} = \log_{10} M_{\text{cut}} + B_{\text{cent}}(x^{\text{rank}} - 0.5), \quad (10)$$

$$\log_{10} M_1^{\text{mod}} = \log_{10} M_1 + B_{\text{sat}}(x^{\text{rank}} - 0.5), \quad (11)$$

where x denotes the secondary property used to trace assembly bias. For LRGs, we use the local environment defined as the mass enclosed within $5h^{-1}\text{Mpc}$ of the halo (excluding the halo itself). For ELGs, we use the local shear as defined in Equation 7 of Hadzhiyska et al. (2022a). The superscript “rank” refers to the normalization procedure where the environment or the shear is ranked amongst halos in each mass bin and then the rank is normalized to a number between 0 and 1. For the shear calculation, we use $R = 0.5 h^{-1}\text{Mpc}$ and a grid size of 1000^3 .

To model central-satellite conformity, we propose a simple model directly inspired by Figure 10. We introduce two extension parameters to the vanilla HOD to model ELG-ELG conformity and ELG-LRG conformity, respectively. Specifically, we modulate the M_1 parameter, which controls the overall amplitude of satellite occupation:

$$M_1^{\text{mod}} = \begin{cases} M_{1,EE} & \text{if ELG central} \\ M_{1,EL} & \text{if LRG central} \\ M_1 & \text{if neither,} \end{cases} \quad (12)$$

where $M_{1,EE}$ modulates the ELG-ELG conformity strength and $M_{1,EL}$ modulates the ELG-LRG conformity strength. This model is more flexible than the maximal conformity model implemented in Rocher et al. (2023), where all ELG satellites are assigned to halos with ELG centrals, which is equivalent to setting $M_1 = \infty$ in our model. This description also effectively distinguishes our conformity model from the galaxy assembly bias model. While the assembly bias model correlates satellite occupation to halo properties and local density, the conformity model only depends on the central galaxy type. Our modeling is also consistent with our proposed physical picture. One can interpret assembly bias as how galaxy color depends on halo assembly history, whereas conformity is largely driven to triggered star formation.²

6.3 Likelihood modeling

For this analysis, we choose the projected 2PCF as our summary statistics. The projected 2PCF marginalizes over the velocity space

² All ABACUSHOD model ingredients referenced in this paper are implemented and released on the official GitHub <https://github.com/abacusorg/abacusutils>.

features of the redshift-space 2PCF, thus removing the need to model galaxy velocities and avoiding potential systematic biases and degeneracies. We compute the projected 2PCF from the galaxy mocks using the fast CORRFUNC code (Sinha & Garrison 2020).

Then we construct a Gaussian log-likelihood function as follows,

$$\log L = -\frac{1}{2} \sum_{i=0}^n \left(\frac{\xi_{i,\text{mock}} - \xi_{i,\text{data}}}{\sigma_i} \right)^2 - \frac{1}{2} \frac{(\bar{n}_{\text{mock}} - \bar{n}_{\text{data}})^2}{\sigma_n^2}. \quad (13)$$

where ξ_i is the i -th of the data vector in consideration. σ_i denotes the jackknife error computed on the data. We ignore the off-diagonal covariances in this analysis because of the small number of jackknife regions and the relatively large data vector. It is also the case that the statistical variance at highly non-linear scales is dominated by shot noise coming from stochastic galaxy occupation, which is de-correlated over scale. We intend to confirm the key findings of this analysis with full covariances when a large data set becomes available. We have also added a term for number density, where σ_n is the uncertainty on the measured mean number density. We assume $\sigma_n/\bar{n}_{\text{data}} = 10\%$ (Yuan et al. 2022b; Guo et al. 2015a).

Having defined our simulations, HOD models, and likelihood functions, we can sample the parameter space to find the best-fit models to the data. We use a global optimization routine called Covariance matrix adaptation evolution strategy (CMA-ES) with 400 random walkers until the walkers converge (Luu 2021). Then we repeat this process 5 times with different random seeds to ensure global convergence.

7 DESI HOD ANALYSIS RESULTS

In this section, we present the main findings of DESI LRG×ELG analyses. First, we fit our extended HOD models on only the LRG×LRG and ELG×ELG auto-correlation functions while using the cross-correlation function as a predictive test. Then, we rerun our fits to also include the cross-correlation function to test the final goodness-of-fit of the favored model.

Because of the large parameter space, a very large number of likelihood calls are needed to achieve convergence in the optimization. To reduce the number of evaluations needed, we perform a two step optimization. First, we optimize the LRG HOD parameters against the LRG auto-correlation function. Then, we fix the LRG HOD parameters at their best-fit values, and we optimize the ELG HOD parameters against the ELG auto-correlation function in section 7.1, or together with the LRG×ELG cross-correlation in section 7.2.

7.1 Auto-only fits

We first compare several different HOD models by fitting the LRG×LRG and ELG×ELG auto-correlation functions. We summarize the fiducial priors in Table 1, and present the goodness-of-fits and model scores in Table 2. The best-fit parameters of the select models are tabulated in Table 3. The best-fit HODs are shown in Figure 13, where the ELG HOD is shown in blue and LRG is shown in orange. The bottom panel shows the best-fit HOD when including conformity, with the dotted line showing the number of satellites in halos with an ELG central and the dashed line showing the number of satellites in halos without an ELG central. We see a very strong conformity effect; the probability of a halo hosting an ELG satellite at fixed halo mass increases by two orders of magnitude when there is a central ELG.

Figure 14 visualizes the best-fit clustering predictions of the vanilla

Bounds	LRG	ELG
$\log_{10} M_{\text{cut}}$	[12, 13.8]	[11.6, 12.6]
$\log_{10} M_1$	[12.5, 15.5]	[12.5, 18.0]
σ	[0.0, 3.0]	[0.0, 3.0]
α	[0.0, 1.5]	[0.0, 1.2]
κ	[0.0, 1.0]	[0.0, 10.0]
p_{max}	-	[0.05, 1.0]
γ	-	[1.0, 15.0]
$\log_{10} M_{1,\text{EE}}$	-	[12.5, 15.5]
$\log_{10} M_{1,\text{EL}}$	-	[12.5, 35.0]
B_{cent}	[-1.0, 1.0]	[-1.0, 1.0]
B_{sat}	[-1.0, 1.0]	[-1.0, 1.0]

Table 1. Prior bounds used for LRG and ELG extended HOD model. We adopt the prior on ELG satellite α from Equation 16. Otherwise, the bounds are chosen to be broad and nonrestrictive. The first 7 rows refer to the vanilla model parameters of the two tracers. The 8-9th rows refer to 1-halo conformity parameters, whereas the last two rows refer to the galaxy assembly bias parameters. Units of mass are in $h^{-1} M_{\odot}$.

Model	Auto-only		Auto+Cross	
	$\chi^2/\text{d.o.f.}$	AIC	$\chi^2/\text{d.o.f.}$	AIC
Vanilla	1.32	56	2.58	132
Vanilla + $M_{1,\text{EE}}$	0.96	48	2.16	114
Vanilla + $M_{1,\text{EE}} + M_{1,\text{EL}}$	0.95	49	2.12	113
Vanilla + $M_{1,\text{EE}} + B^{\text{LRG}}$	-	-	2.15	114
Vanilla + $M_{1,\text{EE}} + B^{\text{ELG}}$	-	-	1.86	102

Table 2. Goodness-of-fit and model AIC scores for our HOD models. The vanilla HOD model refers to the model described from Equation 4–Equation 9. $M_{1,\text{EE}}$ and $M_{1,\text{EL}}$ refer to 1-halo conformity between ELG satellites and ELG centrals and LRG centrals, respectively. See Equation 12 for descriptions. The B^{LRG} and B^{ELG} denote the addition of LRG and ELG assembly bias, respectively. See Equation 11 for definitions. Note that The LRG assembly bias is parameterized in terms of local over-density, whereas the ELG assembly bias is parameterized in terms of local shear.

HOD model in orange and the conformity model in green. The legends in the second panel shows the goodness-of-fits of the two models on the auto-correlation functions, whereas the legends in the third panel shows the significance of the difference between the predicted cross-correlation functions and the data. The error bars are computed from 60 jackknife regions.

We start with vanilla HOD models (“Vanilla” in Table 2, Equation 4–Equation 9), with no assembly bias or conformity. The vanilla model achieves a reasonably good fit on the auto-correlation functions ($\chi^2/\text{d.o.f.}=1.32$) and generates a reasonably consistent prediction of the LRG×ELG cross-correlation function. This is surprising at first glance because from our ILLUSTRISTNG analysis, we expected that a vanilla model without conformity would fail to produce the strong small-scale amplitude of ELG auto-correlation function and the low amplitude of the LRG×ELG cross-correlation function. However, the vanilla model can still produce some of these features via a lowest ELG α value allowed, which assigns a large number of ELG satellite galaxies to low mass halos (see top panel of Figure 13), thus generating excess numbers of ELG pairs with small separation. This is qualitatively consistent with the findings of Rocher et al. (2023), where the authors also found a preference for very small and even negative α in an ELG auto-correlation analysis with vanilla HODs.

Note that our best-fit α is 0.3 whereas [Rocher et al. \(2023\)](#) found a negative α , likely due to the fact that we assign satellites to particles while [Rocher et al. \(2023\)](#) assumed an NFW profile in their vanilla model.

Next, we conduct the equivalent analyses of the auto-correlation functions with our conformity model (“Vanilla+ $M_{1,EE}$ ”, Equation 12). The green curve in Figure 14 shows the best-fit with a vanilla model plus the ELG central-satellite conformity parameter $M_{1,EE}$ as defined in Equation 12. The fit on the two auto-correlation functions achieves an excellent $\chi^2/\text{d.o.f.}$ of 0.96, a significant improvement over the vanilla model. The improvement comes largely from the 1-halo to 2-halo transition regimes at $r_p \sim 0.3h^{-1}\text{Mpc}$, where the conformity model better produces the turnover.

The right panel of Figure 14 shows the cross-correlation predictions from the two models. Neither predictions agree particularly well with the data, though the conformity model reports a smaller χ^2 . On the very small scales, the data sits between the vanilla prediction and the conformity model prediction, but on larger scales both models make consistent predictions that are systematically larger than the data. This suggests that the linear bias of the two tracers are well constrained by the auto-correlations, regardless of whether conformity is included. The systematic difference between the two predictions and the data potentially points to effects such as galaxy assembly bias. As we discussed in section 5.3, hydrodynamical models of DESI samples do support the inclusion of galaxy assembly biases in both the LRG and ELG samples. We will further discuss the inclusion of galaxy assembly bias in the following section on cross-correlation fits.

We also test the addition of ELG×LRG cross conformity parameter $M_{1,EL}$ and report the goodness-of-fitness and AIC scores in Table 2 (“Vanilla+ $M_{1,EE}+M_{1,EL}$ ”). We find that the addition of $M_{1,EL}$ does not significantly improve the fit and the model is disfavored by the data compared to the model with just $M_{1,EE}$. We find the same conclusion in an Auto+Cross fit so we omit $M_{1,EL}$ in the rest of this analysis.

7.2 Auto+cross fits

Similar to the auto-correlation analysis in the previous sub-section, we apply our different HOD models to the auto+cross correlation fits. The goodness-of-fits and model evidence are presented in the last columns of Table 2. The best-fit HODs are shown in Figure 15, and the best-fit parameters are summarized in Table 3. The best-fit predicted clustering are shown in Figure 16.

Immediately, the auto+cross fits confirm the key findings of the auto-only analysis in terms of 1-halo conformity. We find that the inclusion of the conformity parameter $M_{1,EE}$ continues to be favored by data with a significant improvement in $\chi^2/\text{d.o.f.}$, whereas the addition of $M_{1,EL}$ parameter is not favored. Visually, both the “vanilla+confEE” model and the vanilla model continue to produce reasonably good fits on the data. Again the vanilla model can roughly produce the small-scale features with a low α , but it struggles to simultaneously produce the shape of the ELG auto-correlation upturn and the ELG×LRG correlation downturn. The 1-halo to 2-halo transition regime in the ELG auto-correlation function continues to be the most visually discernible difference in the model predictions.

We also test the inclusion of galaxy assembly bias features in the model. Following preceding studies with hydrodynamical simulations and semi-analytic models, we parameterize LRG assembly bias in terms of local scalar environment, whereas we parameterize ELG assembly bias in terms local shear (see section 5.3 for details). As shown in Table 2 under model names “Vanilla+ $M_{1,EE}+B^{\text{LRG}}$ ” and

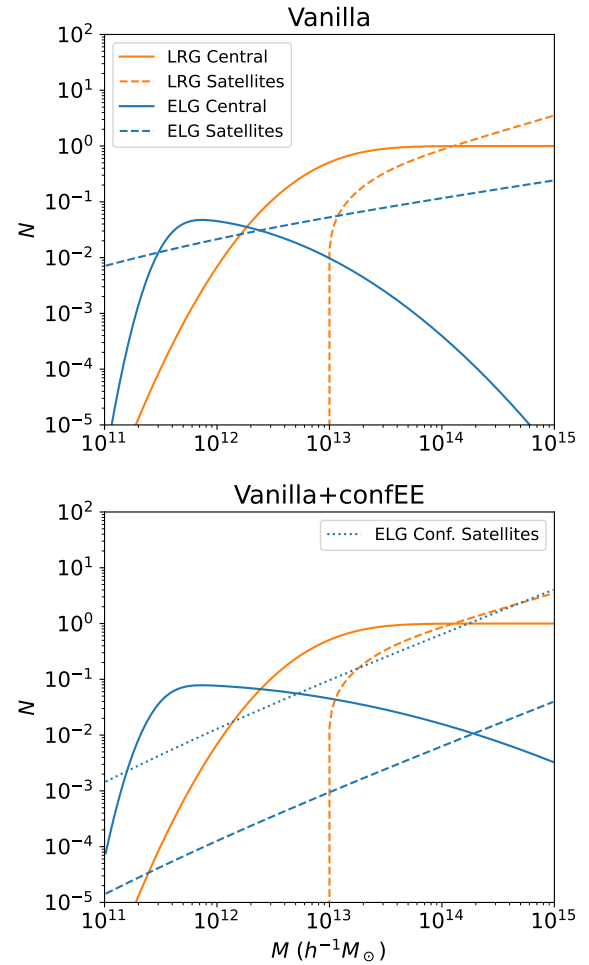


Figure 13. The best-fit HOD of the auto-only fits. The top panel shows the best-fit values of the vanilla model, whereas the bottom panel shows the best-fit values of the vanilla+ $M_{1,EE}$ model. The orange curves denote the HOD of the LRGs while the blue curves denote the HOD of the ELGs. The solid and dashed lines correspond to centrals and satellites, respectively. In the bottom panel, we also show the HOD of the conformal satellites in orange dotted line. The orange dashed line showing the non-conformal satellites goes below the plotted range.

“Vanilla+ $M_{1,EE}+B^{\text{ELG}}$ ”, the addition of LRG assembly bias does not significantly improve the fit on clustering, but the addition of ELG assembly bias does. This result is significant as the first indirect evidence for ELG assembly bias from data. Interpreting the best-fit values in Table 3, the ELG centrals slightly prefer lower shear environments, whereas the satellites prefer higher shear environments.

The combination of a strong central-satellite conformity signal and a preference for high-shear environments in the satellites is again consistent with the picture that the ELGs preferentially select tidally disturbed galaxies undergoing mergers and displaying triggered star formation at the time of observation. We do not yet know the significance of our assembly bias constraints without proper posterior sampling. We reserve a more comprehensive exploration of ELG assembly bias for a future analysis.

An interesting discrepancy in these fits is in the ELG satellite fraction. While the vanilla model predicts a rather large ELG satellite fraction of 30–50%, the conformity model produces a low satellite fraction at 2–10%. In comparison, for eBOSS ELGs, [Guo et al. \(2019\)](#)

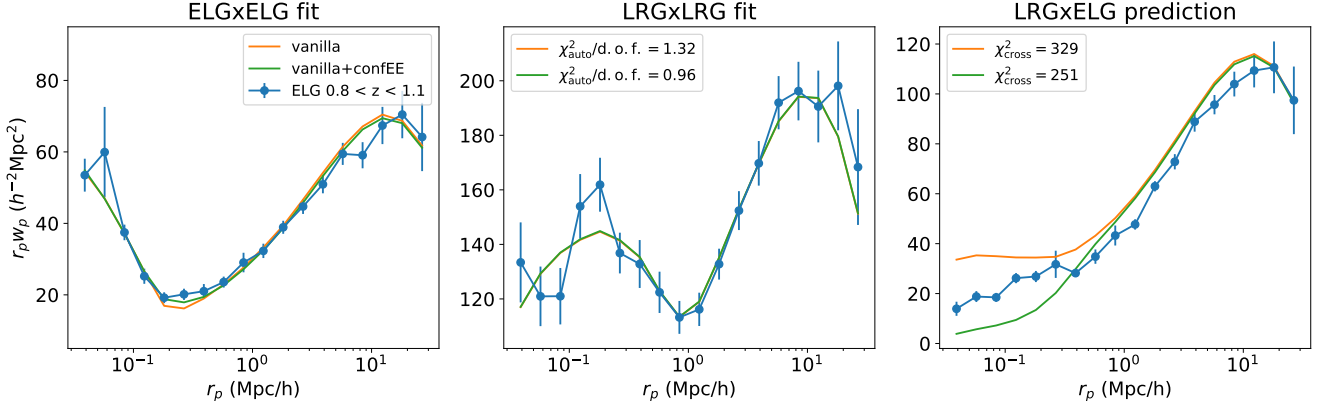


Figure 14. Best-fits on the DESI One-Percent auto-correlation functions using the vanilla HOD model and the vanilla+ $M_{1,EE}$ conformity model. For this comparison, we are only fitting the ELG×ELG and LRG×LRG auto-correlation functions. The LRG×ELG cross-correlations shown for the two models are blind predictions. Also note that we are fitting LRG HOD on the LRG auto-correlation first and then fixing the LRG HOD parameters when fitting ELG HOD parameters. Thus, the orange and green curves in the second panel fully overlaps. The vanilla model achieves a best-fit $\chi^2/\text{d.o.f.} = 1.32$ on the auto-correlation functions, whereas the vanilla+ $M_{1,EE}$ model achieves $\chi^2/\text{d.o.f.} = 0.96$. On the cross-correlation function, the vanilla model yields a $\chi^2 = 329$, whereas the vanilla+ $M_{1,EE}$ model yields $\chi^2 = 251$.

Tracer	Parameters	Vanilla (Auto)	Vanilla + $M_{1,EE}$ (Auto)	Vanilla (Auto+Cross)	Vanilla + $M_{1,EE}$ (Auto+Cross)	Vanilla + $M_{1,EE}$ + B^{ELG} (Auto+Cross)
LRG	$\log M_{\text{cut}}$	12.98	12.98	12.98	12.98	12.98
	$\log M_1$	14.06	14.06	14.06	14.06	14.06
	σ	0.40	0.40	0.40	0.40	0.40
	α	0.59	0.59	0.59	0.59	0.59
	κ	1.00	1.00	1.00	1.00	1.00
	f_{sat}	0.097	0.097	0.097	0.097	0.097
	$\log_{10} \bar{M}$	13.22	13.22	13.22	13.22	13.22
ELG	$\log M_{\text{cut}}$	11.58	11.50	11.50	11.50	11.64
	$\log M_1$	16.98	16.75	17.97	16.12	15.17
	σ	0.77	1.37	0.75	0.42	1.04
	α	0.31	0.79	0.30	0.48	0.70
	κ	0.34	0.33	0.11	1.30	0.18
	p_{max}	0.06	0.15	0.07	0.06	0.33
	γ	5.17	8.62	5.37	4.78	5.60
	$\log_{10} M_{1,EE}$	-	14.21	-	14.46	14.44
	B_{cent}	-	-	-	-	0.14
	B_{sat}	-	-	-	-	-0.42
	f_{sat}	0.525	0.023	0.314	0.107	0.102
$\log_{10} \bar{M}$	11.98	12.07	11.91	11.98	12.23	

Table 3. LRG and ELG best-fit parameters. We also quote the marginalized satellite fraction f_{sat} and the sample completeness f_{ic} . Units of mass are given in $h^{-1} M_{\odot}$.

found a satellite fraction of 13–17%, whereas Favole et al. (2016) found a satellite fraction of $22.5 \pm 2.5\%$. These studies used vanilla models without conformity as eBOSS clustering measurements were not sufficiently precise on the very small scales to detect potential signatures of conformity. In more recent DESI analyses, Rocher et al.

(2023) found a similar satellite fraction of 2.3% when including maximal conformity but assuming a slightly different vanilla model. Yu et al. (2023) analyzed the same data with a sub-halo abundance matching model and also found a low satellite fraction for ELGs, at 3–5% depending on the specifics of the model. However, Gao

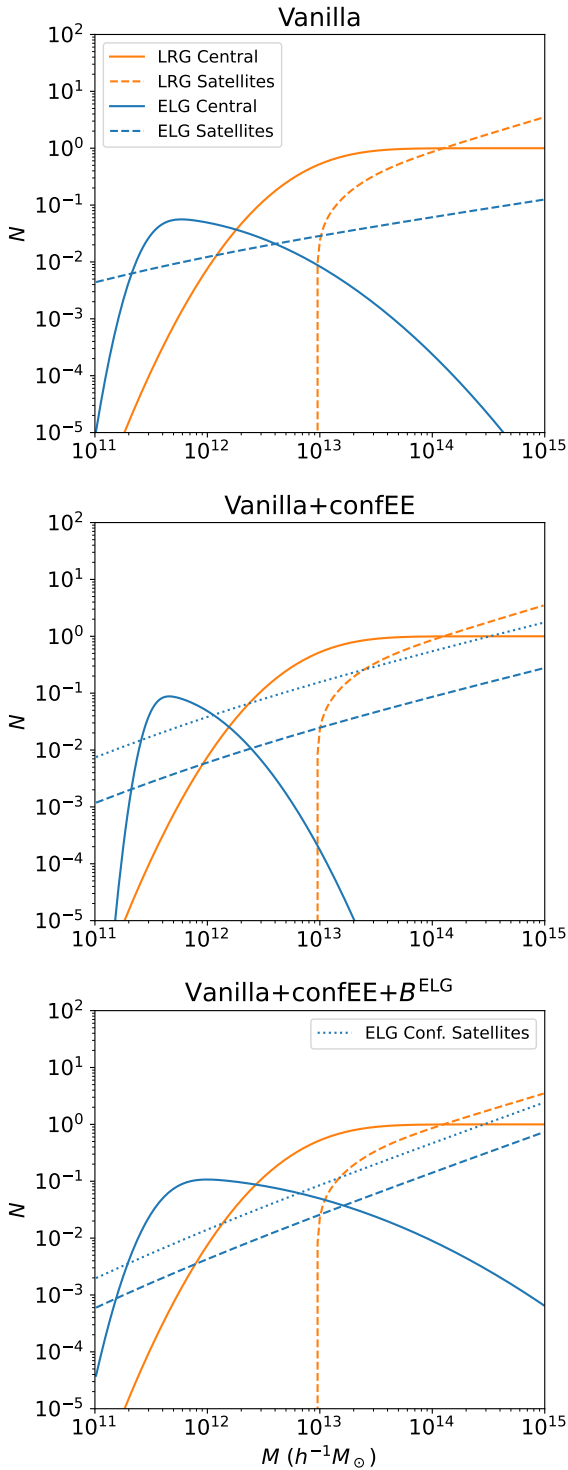


Figure 15. The best-fit HOD of the auto+cross fits. The top to bottom panels show the best-fit values of the vanilla model, the vanilla+ $M_{1,EE}$ model, and the vanilla+ $M_{1,EE}+B^{ELG}$ models, respectively. The orange curves denote the HOD of the LRGs while the blue curves denote the HOD of the ELGs. The solid and dashed lines correspond to centrals and satellites, respectively. The dotted blue lines show the HOD of the conformal satellites.

et al. (2023b) also used a SHAM model to predict the auto- and cross-correlation functions and found a satellite fraction of $\sim 15\%$, higher than the other DESI analyses. These comparisons suggest that a combination of features specific to the DESI sample and the inclusion of conformity in the modeling potentially contributed to a low satellite fraction, but there are still some disagreements between the different methods.

It makes sense that conformity reduces the predicted satellite fraction as it accounts for the excess small-separation pairs through tight central-satellite pairs, whereas the vanilla model produces the small-scale signature by producing large numbers of satellites in small halos by preferring a low α . One caveat is that a low α produces satellites in small halos without centrals, which cannot be effectively distinguished from centrals with clustering alone. In other words, we can simply re-label satellites without centrals as centrals and it would result in the same clustering prediction, or that the satellite fraction is somewhat degenerate with the definition of centrals and satellites in these small halos. Avila et al. (2020) found a similar conclusion with eBOSS data that the inferred ELG satellite fraction varies with the assumed HOD model, anywhere between 20-50% for their models.

Overall, we find some statistical evidence that the inclusion of conformity and galaxy assembly bias in the ELG HOD are favored by the observed auto and cross-correlation functions. This is consistent with the physical picture of triggered starburst we proposed in section 3 and the conformity signal we find in ILLUSTRISTNG in section 5. However, we continue to find that the vanilla model can produce a reasonably good fit to the clustering by generating a large number of ELG satellites in small halos with a low α , and that the improvement when including conformity and galaxy assembly bias is not particularly visually obvious in the clustering comparisons. Thus, a more rigorous statistical comparison of the models are needed to quantify the model evidences. Our results are meaningful as part of a broader push on ELG modeling, and we reserve a more complete HOD analysis for the future.

Our model also ultimately did not produce $\chi^2/\text{d.o.f.} \approx 1$ on the auto+cross fit. This could be due to the fact that we do not consider the full covariance matrix for this analysis due to limited number of jackknife regions. We speculate that positive off-diagonal terms would reduce the significance of model discrepancies and reduce the overall χ^2 . On the modeling side, we have ignored redshift evolution, which can prove important as we push towards $\chi^2/\text{d.o.f.} = 1$.

There is also the possibility of additional motivated extensions to the HOD model. Rocher et al. (2023) proposed the inclusion of an extended halo profile. Specifically, their default model assigned ELG satellite galaxies according to an NFW profile, but they found that a modified NFW profile allowing satellite galaxies to be assigned further away from the halo center is significantly reduced the χ^2 . The extended profile is motivated by the notion that star-forming galaxies are quickly quenched when they fall deep into the halo potential well. There are several lines of observational evidence showing the quenched fraction of galaxies is indeed radially dependent within a halo in SDSS (Wetzel et al. 2012; Blanton & Berlind 2007), but the connection between those observations and high redshift ELGs is unclear and we did not find evidence of deviations from NFW profile in ELGs in hydrodynamical simulations (Hadzhiyska et al. 2022a; Yuan et al. 2022b). We suggest a detailed study of ELG radial distributions in the future.

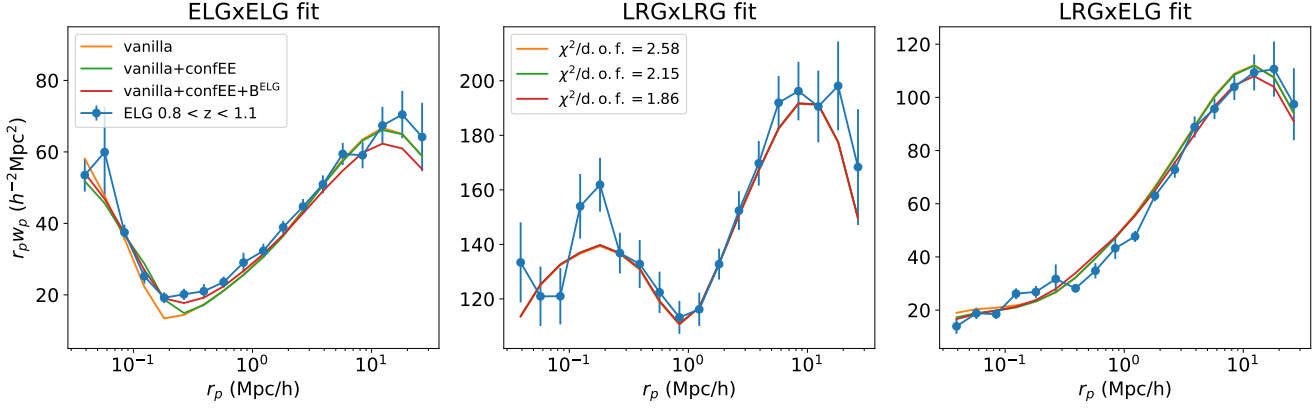


Figure 16. Best-fits on the DESI One-Percent auto and cross-correlation functions using the vanilla HOD model, the vanilla+ $M_{1,EE}$ model, and the vanilla+ $M_{1,EE}+B^{ELG}$ models. For this comparison, we are fitting the all three auto and cross-correlation functions.

8 CONSTRAINTS FROM CLUSTER CROSS-CORRELATIONS

Given the degeneracy between conformity and low satellite occupation power-law index α seen in this analysis and in [Rocher et al. \(2023\)](#), observables that can directly constrain α become particularly interesting. In this section, we present one such observable, where we tabulate DESI ELG satellite counts around known galaxy clusters. Combined with the independently measured cluster richness-mass relationship, this gives us a direct way to constrain the ELG satellite α in massive halos and potentially break this degeneracy.

We use the Legacy Survey redMaPPer cluster catalog ([Ider Chitham et al. 2020](#)). redMaPPer is a red-sequence photometric cluster finding algorithm that identifies galaxy clusters as over-densities of red galaxies, and estimates the probability that each red galaxy is a cluster member following a matched filter approach that models the galaxy distribution as the sum of a cluster and background component. A richness parameter λ is computed for each cluster and is defined the sum total of the membership probabilities of all the galaxies. It has been found that richness λ tightly correlates with the total mass of the cluster (recent examples include [McClintock et al. 2019](#); [Simet et al. 2017](#); [Baxter et al. 2016](#)), thus giving us a way to directly relate ELG occupation to halo mass.

The Legacy Survey redMaPPer cluster catalog is obtained by running redMaPPer on DR9 photometry from the DESI Legacy Imaging Surveys ([Dey et al. 2019](#)), covering approximately 14,300 deg². For our analysis, we select 2490 clusters that are fully within the DESI SV3 footprint and have spectroscopically confirmed Bright Central Galaxies (BCGs) in DESI. Specifically, we only consider clusters whose centers are within the SV3 footprint and their distances to the edge of footprint is at least 0.22 degrees, which translates to a comoving distance of 9.4 h^{-1} Mpc at $z = 1$. This procedure removes the need to consider boundary effects. We use DESI spectroscopic redshift measurements (spec- z) for the BCGs as the cluster redshifts to partially remove the need to consider cluster redshift uncertainty and associated projection effects. We further remove clusters with richness $\lambda < 5$ to reduce our exposure to systematics due to richness bias, resulting in 1447 clusters for our final sample.

To compute the ELG satellite count as a function of cluster mass, we first search for ELG neighbors in 2D around each cluster in a radius that is 3 times the default richness-dependent redMaPPer radius. The number 3 is chosen to roughly reproduce the expected R_{200m} around a $10^{14} h^{-1} M_{\odot}$ halo with richness ~ 10 . We only select ELG

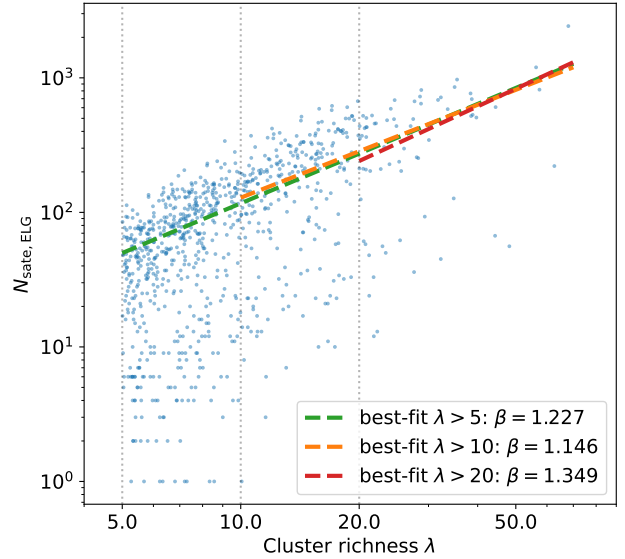


Figure 17. The number of DESI ELG satellites per redMaPPer cluster as a function of cluster richness. The blue points show the individual clusters. The three dashed lines show the power law fits through clusters with different minimum richness cuts. The power law slope measurement varies by $\sim 20\%$. The statistical uncertainty on the best-fit β is below 0.001 in all three cases.

neighbors within a finite cylinder along the line-of-sight, centered on the BCG spec- z . Specifically, for each cluster with spectroscopic redshift z_{BCG} , we only include ELGs within redshift range $z_{BCG} \pm 3(\sigma_v/c)$, where σ_v is the cluster velocity dispersion. The velocity dispersion measurement is fairly uncertain, so we set the velocity dispersion measurements to both 500km/s and 1000km/s, and we find that the two different values result in a $\sim 1\%$ change in the ELG satellite counts. Considering that we are using spec- z for clusters and the robustness of satellite counts to the choice of velocity dispersion, our results should be robust to projection effects in the cluster-ELG pair counts.

Figure 17 shows the number of ELG satellites as a function of cluster richness. The blue points showcase the sample distribution. The dashed lines show the best-fit power law with increasing minimum λ . Clearly, we see an monotonically increasing trend, suggesting higher

richness clusters (more massive halos) host more ELG satellites. This strongly rejects a negative ELG α , in which case less massive halos host more ELG satellites. To further quantify this measurement, we define the satellite-occupation vs. richness correlation parameter β , as in

$$N_{\text{sate,ELG}} \sim \lambda^\beta. \quad (14)$$

The dashed green line shows the fit to the full cluster sample ($\lambda > 5$), resulting in best-fit $\beta = 1.23$.

However, the optical richness of redMaPPer clusters can be subject to large biases due to projection effects in cluster member assignments (Rozo et al. 2015; Costanzi et al. 2019; Sohn et al. 2018; Sunayama et al. 2020). Myles et al. (2021) showed that this bias can be as large as 20% and increases with lower richness and higher redshift. Unfortunately, we do not currently have measurements of this bias for clusters at $z \sim 1$. For the purposes of this fairly qualitative analysis, we conduct an internal consistency check by measuring β for progressively larger minimum richness. These measurements are shown with dashed orange and red lines in Figure 17. The best-fit β is self-consistent at $\pm 10\%$, varying between 1.15 and 1.35. This potentially demonstrates that our β measurements are not strongly affected by richness bias, especially considering $\lambda > 20$ was employed for the fiducial cosmology analysis in Abbott et al. (2020) and Costanzi et al. (2021). Nevertheless, we acknowledge that with current data it is not currently feasible to explicitly calculate richness bias for our sample and that the richness values used in our analysis can still be significantly affected by projection effects.

To translate constraints on β to α in the HOD, we need to know the power law index in the cluster mass-richness relationship. For redMaPPer clusters, recent studies have used clustering and weak lensing to directly constrain cluster masses and derive mass-richness relationships. At lower redshift $z < 0.33$, Simet et al. (2017) derived $M \sim \lambda^{1.3 \pm 0.1}$ from weak lensing measurements, whereas Baxter et al. (2016) derived $M \sim \lambda^{1.2 \pm 0.2}$ from clustering measurements. McClintock et al. (2019) uses DES Y1 imaging to calibrate redMaPPer mass-richness relationship up to $z = 0.65$, deriving $M \sim \lambda^{1.35 \pm 0.13}$. Murata et al. (2019) used HSC imaging to study the redshift evolution of the mass-richness relationship of the CAMIRA clusters and found the power law index to be insensitive to redshift at $z < 1$. Combining these results, we suggest a conservative mass-richness relationship of

$$\lambda \sim M^{0.7-0.9}. \quad (15)$$

Combining Equation 15 and our range for β , we arrive a range for the satellite power index α that is

$$0.8 < \alpha < 1.2. \quad (16)$$

This range is broadly consistent with recent MilleniumTNG studies and semi-analytic models (Hadzhiyska et al. 2022a; Yuan et al. 2022b; Avila et al. 2020). This range favors models with higher inferred α , such as the Vanilla+ $M_{1,EE}$ (auto) and Vanilla+ $M_{1,EE}+B^{\text{ELG}}$ (cross) models in Table 3. It disfavors vanilla models that require a much lower $\alpha = 0.3$ to describe the clustering. Moreover, this measurement strongly disfavors the vanilla models in Rocher et al. (2023) that require a negative α .

Finally, we re-iterate that while we have attempted to minimize systematic biases in this exercise by conducting self-consistency tests and employing spectroscopic redshifts whenever possible, our results can still be affected by a range of systematics related to optical richness including projection effects and mis-centering. Nevertheless, this result is important as a first step in breaking the degeneracy between low α and conformity models.

9 PRODUCING CONFORMITY WITH UNIVERSEMACHINE

So far, we have motivated the inclusion of conformity through both hydrodynamical models and observations. We have also used COSMOS data to build a physical picture for the ELGs that should naturally generate conformity. In this section, we explore the origin of ELG conformity through a set of tests with UniverseMachine.

Specifically, we stress test the UniverseMachine model by varying its parameters to see if it can consistently predict the DESI ELG stellar mass function, SFR distribution, and clustering. Our tests challenge a fundamental assumption in UniverseMachine that ties galaxy SFR exclusively to halo mass and halo mass assembly history. We argue that the type of conformity signal we see requires a more flexible star formation model that includes additional merger-triggered starburst that is independent of mass assembly. These tests also further distinguish merger-triggered conformity from galaxy assembly bias.

9.1 UniverseMachine model

UNIVERSEMACHINE (UM; Behroozi et al. 2019a) is an empirical galaxy-halo connection model that predicts galaxy star formation rates from halo mass and halo assembly histories. It is a flexible framework that models the full evolution histories of galaxies anchored on dark matter halo merger trees from cosmological simulations, and it is simultaneously constrained by observed galaxy stellar mass functions, UV luminosity functions, quenched fractions, cosmic star formation history, and galaxy clustering over a wide range of galaxy mass and redshifts (up to $z \sim 8$). The galaxy clustering constraints included in Behroozi et al. (2019a) were from SDSS DR7 (Kauffmann et al. 2003; Brinchmann et al. 2004; Abazajian et al. 2009) that cover auto and cross correlations of all, quenched, and star-forming galaxies with $M_* > 10^{10.3} M_\odot$ at $z < 0.7$.

We briefly summarize the UM model framework. The model uses peak halo maximum circular velocity, v_{Mpeak} , as a halo mass proxy that is both resistant to pseudo evolution and consistent for either satellites and centrals. The model parameterizes the redshift-dependent mean star formation rate and galaxy quenched fractions (f_Q) as a function of v_{Mpeak} (with some parameterized intrinsic scatter). These parameterizations determine the distribution of galaxy SFRs in each redshift and halo mass bin (double Gaussian normalization ratio given by f_Q). In each halo mass (v_{Mpeak}) bin, the model tends to map higher SFR onto earlier-forming halos with lower recent accretion rates, capturing the effect of halo assembly bias. The halo recent accretion rate at each redshift (z) is defined as (Behroozi et al. 2019a):

$$\Delta v_{\text{max}}(z) = \frac{v_{\text{max}}(z)}{v_{\text{max}}(\max(z_{\text{dyn}}, z_{\text{Mpeak}}))}, \quad (17)$$

with z_{dyn} being the redshift one dynamical timescale ago from z and z_{Mpeak} being the redshift of peak halo mass. For each halo, its SFR is determined by a percentile rank function:

$$C(\text{SFR}) = C \left(r_c C^{-1}(C(\Delta v_{\text{max}})) + \sqrt{1 - r_c^2} R(t) \right), \quad (18)$$

where $C(x) = 0.5 + 0.5\text{erf}(x/\sqrt{2})$ is the cumulative percentile rank function. r_c is the rank correlation coefficient between the percentile rank in SFR and percentile rank in Δv_{max} in each halo v_{Mpeak} bin (dependent on v_{Mpeak} and z). r_c controls the strength of the correlation between SFR and halo accretion, while the random series $R(t)$ contributes a time-correlated piece. The random time series is

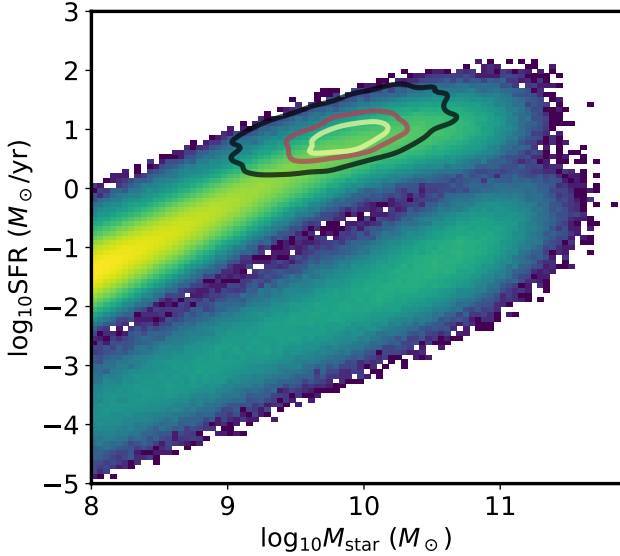


Figure 18. The distribution of UniverseMachine galaxies in the stellar mass and star formation rate plane, compared to the mock ELGs shown in contours. We have applied a shift of -0.2 dex to $\log_{10}\text{SFR}$ and 0.2 dex to $\log_{10} M_{\text{star}}$ of the COSMOS ELGs to better match the UM stellar mass vs SFR distribution.

parameterized as:

$$R(t) = f_{\text{short}} S_{\text{short}}(t) + \sqrt{1 - f_{\text{short}}^2} S_{\text{long}}(t), \quad (19)$$

where $S_{\text{short}}(t)$ is an uncorrelated unit random variable that models the short-timescale stochasticity of the SFR. $S_{\text{long}}(t)$ is a correlated random Gaussian series with correlation timescale set to the dynamical timescale (correlation coefficient for two time steps separated by δt is $\exp(-\delta t/\tau_{\text{dyn}})$). Finally, f_{short} is the parameter that models the relative proportion of short versus long timescale variations of SFR.

9.2 Mimicking ELG conformity

Within the existing UM model, r_c and f_{short} fully control the assignment of SFR at given halo mass and given set of halo accretion rates. Hence these two parameters should fully determine any emergent galaxy assembly bias and conformity. For example, larger r_c means stronger correlation between galaxy SFR and halo assembly history at fixed halo mass, resulting in strong galaxy assembly bias by definition. We also expect a large r_c to result in stronger conformity because of the correlated assembly histories of host halo and its subhalos. However, based on the analyses in this paper, we postulate that 1-halo conformity can be potentially attributed to merger-triggered starburst in addition to correlated halo accretion. A SFR model that purely depends on halo mass and recent accretion would not predict the additional star formation triggered by galaxy mergers, which requires an additional dependency on local tidal field or proximity to other galaxies. Thus, by flexing the UM model parameters and testing whether the current UM model space can produce the type of conformity signal we see in DESI, we can determine whether the correlated halo accretion alone can explain the conformity signal we see in DESI and elucidate the distinction between ELG conformity and galaxy assembly bias.

We run three UM models: (1) The fiducial model with default parameters reported in Behroozi et al. (2019b) ($r_c = 0.5$, $f_{\text{short}} = 1$);

(2) A model where we set $f_{\text{short}} = 0.5$ to reduce the proportion of short timescale variations in SFR, i.e. making the star formation history more correlated on long time scales; (3) A model where we set $r_c = 1$ to obtain maximum correlation between SFR and assembly history. Comparing model (2) and (3) to the fiducial model (1) allows us to test which aspect, if any, of the SFR model can be tweaked to produce the ELG clustering we observe. We run all three models on a $250h^{-1}\text{Mpc}$ N-body simulation box with 2560^3 particles and particle mass $7.4 \times 10^7 h^{-1} M_{\odot}$. The simulation is run with L-GADGET2 code at a fiducial ΛCDM cosmology of $\Omega_m = 0.286$, $\Omega_b = 0.047$, $\sigma_8 = 0.82$, $n_s = 0.96$, $h = 0.7$ (Wang et al. 2021; Becker 2015; Mao et al. 2015; Springel et al. 2005). We use the $z = 0.8$ snapshot.

We select ELGs in the UM boxes by directly matching the 2D stellar mass vs. SFR distribution of DESI ELGs in COSMOS (Figure 5). The 2D histograms in Figure 18 show the stellar mass and SFR distribution of the full UM catalog at $z = 0.8$. The contours visualize the selected ELGs. We have shifted the COSMOS SFR and stellar mass by -0.2 dex and 0.2 dex, respectively, to better match the values in UM. Such systematic shifts could be necessary due to differences in mass definition or systematics in masses inferred from SED fitting, but the point is that the ELGs are located in qualitatively the same region of parameter space as in Figure 5. We repeat the same selection over the three UM models. Also note that because we are explicitly matching the stellar mass and SFR distribution in the mock ELG selection, the only observable we need to match when we vary the UM parameters is the clustering.

Figure 19 displays the HODs of the selected mock ELGs in the three UM models. The solid blue curves show the HOD of the centrals, whereas the orange curves show the HOD of the ELG satellites. Upon first glance, the three different models produce remarkably consistent ELG HODs that are also qualitatively consistent with our inferred HODs from DESI (Figure 13 and Figure 15) and also the ILLUSTRISTNG prediction in Figure 10. The satellite HODs report a power index of $\alpha \sim 0.9$, somewhat larger than the prior range we set from redMaPPer analysis (Equation 16), but nonetheless disfavors the vanilla HOD models that infer very low α values. The dotted and dashed lines show the HOD of ELG satellites in halos with and without and ELG centrals. Clearly, none of the three models produce a large number of conformity, unlike in ILLUSTRISTNG and we inferred from data. The $r_c = 1$ model produces a larger fraction of satellites with ELG centrals at 7% as opposed to 2% in the fiducial and $f_{\text{short}} = 0.5$ models. This makes sense as $r_c = 1$ maximally ties SFR to recent accretion history, resulting in some conformity effect. Nevertheless, the weak conformity across the three models suggests that SFR correlated halo accretion as modeled in UM creates a small but insufficient amount of conformity.

We find the same conclusion when looking at the clustering signatures. Figure 20 showcases the predicted ELG 2PCF from our UM ELG selection compared to the DESI measurement. The three panels correspond to the three different UM models. We also show in dashed curves the 2PCF prediction when we shuffle satellite galaxies among halos of the same mass, which removes any central-satellite conformity.

In the left panel showing the fiducial model prediction, we match the observed clustering between $0.2-10h^{-1}\text{Mpc}$. At larger r_p , the deviation likely comes from sample variance and missing large scale modes. At smaller r_p , the fiducial UM model does not predict the upturn that is indicative of conformity. The middle panel shows that reducing short time scale uncorrelated fluctuation in the star formation history does not have a significant effect on the projected 2PCF. The right panel shows that increasing r_c to 1 does produce

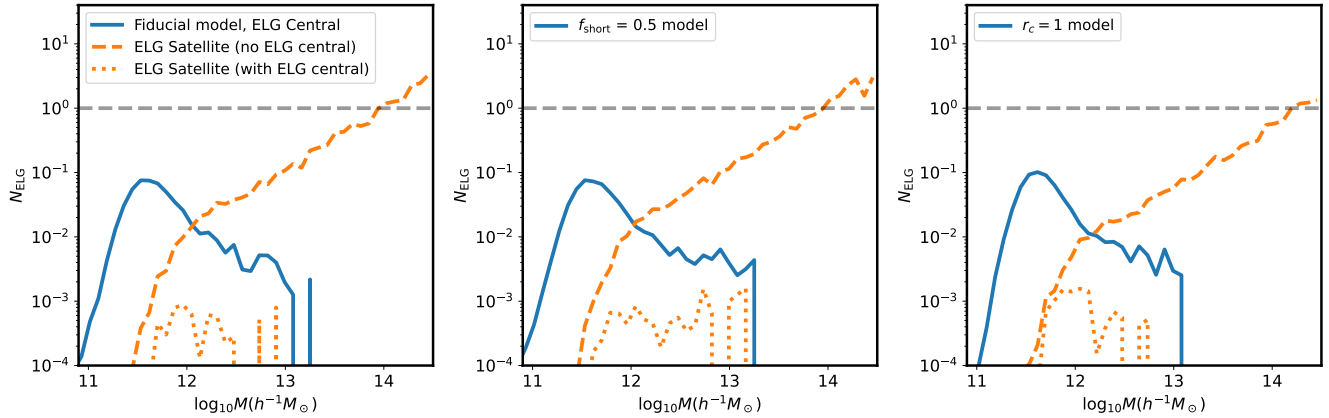


Figure 19. HODs of UniverseMachine ELGs selected by sampling the ELG stellar mass function and star formation rate distribution in COSMOS. The three panels correspond to the fiducial model, the model where we set $f_{\text{short}} = 0.5$, and the model where we set $r_c = 1$. The blue solid lines show the central HOD, whereas the satellites are shown in orange. We separate the satellites into satellites in halos with ELG centrals (in dotted), and satellites in halos without ELG centrals (in dashed). None of the three models generated as much conformity as we saw in ILLUSTRISTNG or in the DESI analysis.

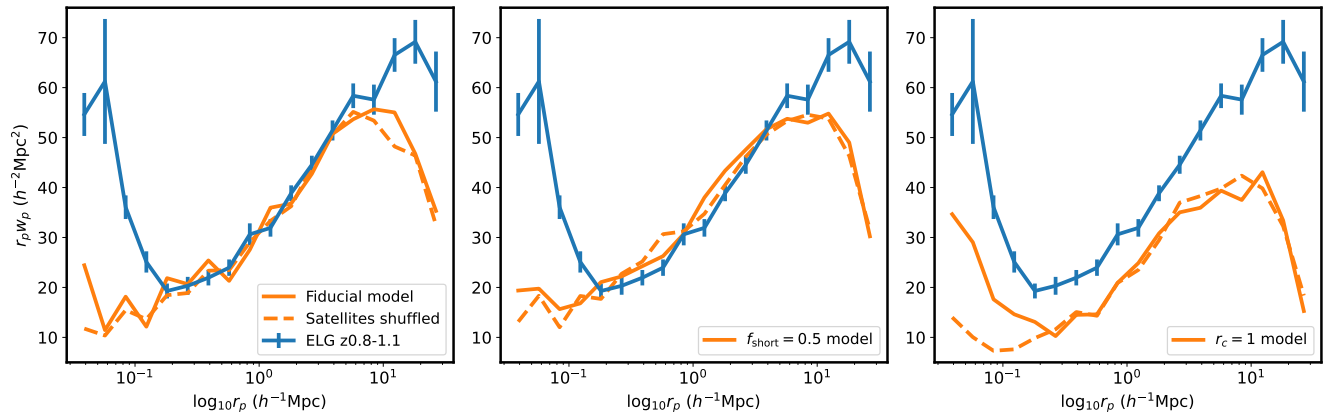


Figure 20. The projected 2-point auto-correlation function of UniverseMachine ELGs (in orange) compared to the DESI measurement (in blue). The three panels correspond to different UniverseMachine models. The dashed lines show the clustering when we shuffle satellites amongst halos of the same mass, removing 1-halo conformity. Only the $r_c = 1$ model in the last panel produced a noticeable conformity signature.

some excess clustering on small scales, though not strong as in data. The dashed line shows that the upturn is indeed due to central-satellite conformity. However, setting $r_c = 1$ breaks the consistency in clustering amplitude on large scales. This is not surprising as $r_c = 1$ maximally associates star formation with recent growth, generating a large amount of galaxy assembly bias as result, which modulates the galaxy clustering on 2-halo scales. Because the large scale clustering in UM is well constrained with existing data, a $r_c = 1$ model that significantly changes the large-scale clustering predictions is strongly disfavored.

Before we move on, we point out that it is possible that our ELG selection in UM is not realistic and that an actual SED based selection would report significantly different clustering on 1-halo scales. However, we find that a stellar mass and SFR based selection on ILLUSTRISTNG still results in a strong conformity signal (we omit that discussion for brevity). Similarly, we tested a range of stellar mass and SFR based selection for ELGs in UM, and failed to find a selection that produces significant conformity while also predicting the right number density and stellar mass function. We believe that the lack of conformity in UM cannot be entirely due to selection, but we advocate for a more thorough examination in future work.

To summarize, while we could generate some conformity signal by maximally correlating SFR with recent accretion history, it does so by breaking consistency in the ELG 2PCF on 2-halo scales. This suggests that the UM model is not currently flexible enough to describe the ELG sample down to 1-halo scales. This makes sense given our physical picture of ELG star formation being at least partially triggered by tidal interactions, whereas UM only correlates star formation with mass assembly, not environmental triggers. Modeling triggered star formation in UM would essentially require modifying Equation 18 by adding an association between SFR with local tidal field or the existence and types of neighboring galaxies. We intend to implement such a model extension in the future.

10 DISCUSSION

In this paper, we have pushed on our understanding of ELGs and argued for the inclusion of conformity through both observations and physical models. To complement our results, we survey the literature for other studies of ELG conformity and compare with our analysis. We also examine alternative theories on the origin of conformity.

10.1 ELG conformity in the literature

This paper expands significantly on the analysis of [Rocher et al. \(2023\)](#), by leveraging cross-correlations and external datasets to build a clearer physical picture of the DESI ELG sample. [Rocher et al. \(2023\)](#) did not find a clear preference for conformity in terms of ELG auto-correlation data alone because of a strong degeneracy between conformity and small α . Specifically they found that an HOD with conformity results in an α of 0.7-0.9, whereas the model without conformity favors a value of $\alpha = -0.26$. We presented several pieces of evidence that disfavor a negative α , including our tests with ILLUSTRISTNG and UM, and the cross-correlation of ELG satellites with redMaPPer clusters.

[Gao et al. \(2023a\)](#) analyzed the DESI LRG \times ELG measurements in a subhalo abundance matching (SHAM) framework instead of an HOD. They similarly found that the vanilla SHAM model fails to predict the small-scale clustering of ELGs, and that an extended SHAM model with 1-halo conformity is strongly preferred by the data. This is highly complimentary to our study by showing that the preference for conformity is not simply due to potential limitations of the HOD, but a feature that requires a physical explanation. However, the same paper does not find a need for galaxy assembly bias in order to describe the auto+cross correlation functions. This is likely because SHAM already incorporates at least some galaxy assembly bias, as subhalos readily encode halo assembly information ([Chaves-Montero et al. 2016](#)).

There is also evidence for the need of explicit conformity model in an HOD framework before DESI. [Ross & Brunner \(2009\)](#) analyzed the small-scale clustering of red and blue galaxies in SDSS DR5 and found that a vanilla model that fully mixes the blue and red galaxies does not fit the data, whereas a model that segregates blue and red galaxies into distinct halos (akin to conformity) does. Additional evidence of conformity in red vs blue galaxies was also seen in the Deep Extragalactic Evolution Probe (DEEP2) spectroscopic survey ([Newman et al. 2013](#)). Specifically, [Coil et al. \(2008\)](#) showed that the projected clustering of blue galaxies at $0.7 < z < 1.2$ shows a strong upturn on very small scales, which is not produced by a vanilla HOD fit ([Tinker & Wetzell 2010](#)). While these studies did not attempt a conformity model, the clustering signatures are fully consistent with what we expect from ELG conformity. Similarly, 1-halo conformity at high redshift was also observed in the UKIRT Infrared Deep Sky Survey (UKIDSS; [Lawrence et al. 2007](#); [Hartley et al. 2015](#); [Kawinwanichakij et al. 2016](#)).

10.2 Origin of conformity

A key motivation of this paper is to postulate merger-triggered starburst as a new mechanism for conformity. Another piece of evidence supporting this model comes in [Hadzhiyska et al. \(2022a\)](#), where the authors studied the clustering of mock $z = 1$ ELG and LRGs in MILLENIUMTNG. The study found strong signatures of 1-halo conformity, i.e., that ELG satellites preferentially occupy halos with ELG centrals. The study also found evidence for anisotropic distribution of ELG satellites within halos, specifically that ELG satellites preferentially exist in close proximity with each other. The authors argued that a ‘‘cooperative star formation’’ scenario can naturally explain the conformity signal seen in MILLENIUMTNG, which is consistent with our picture of merger-triggered starburst.

Prior to this study, conformity is widely believed to originate from spatially correlated halo accretion. [Hearin et al. \(2016b\)](#) found clear spatial correlation in halo accretion in simulations and postulated that the conformity up to $4h^{-1}$ Mpc seen in SDSS is a result of SFR being

correlated with halo accretion. The same work proposed that 1-halo conformity is simply a result of 2-halo conformity at higher redshift. However, this hypothesis also showed that halo accretion correlation also decreases precipitously at higher redshift, thus it would struggle to explain the strong 1-halo conformity we see at $z \sim 1$. This echoes our finding in section 9 that tight correlation of SFR to halo accretion rate does not generate sufficient conformity to explain data.

Several other studies attempted to explain 1-halo conformity via direct interactions between central and satellite galaxies. [Hartley et al. \(2015\)](#) studied the conformity signal between quiescent galaxies and argued that a star formation (or active galactic nucleus) related outburst event from the central galaxy could establish a hot halo environment which is then capable of quenching both central and satellite galaxies. [Wang & White \(2012\)](#) similarly argued that massive red centrals preferentially live in halos with excess hot gas and massive central black holes, making them more efficient at quenching satellite galaxies. There have also been a series of papers studying mechanisms for the more contested 2-halo conformity effect, including pre-heating by early generations of black holes ([Kauffmann 2015](#)), a combination of systematic biases ([Sin et al. 2017](#)), and modified halo mass quenching model ([Zu & Mandelbaum 2018](#)). These mechanisms might prove relevant for 1-halo conformity as well, but we leave that to a future study.

10.3 Implications on merger–SFR connection

Galaxy mergers and tidal interactions form a key part of our understanding of how galaxies form and grow. Yet there exists an active debate as to whether or how mergers trigger star formation. While studies such as [Ellison et al. \(2013\)](#); [Knapen et al. \(2015\)](#) found mergers to suppress star formation, others found mergers to trigger periods of rapid star formation and even starbursts (e.g. [Saitoh et al. 2009](#); [Horstman et al. 2021](#)). More recently, [Renaud et al. \(2022\)](#) suggested that the merger–star formation connection is dependent on the stage of evolution and can only occur after the formation of the galactic disk. Our analysis uniquely contributes to this discussion by combining information from spectra, imaging, and clustering. Our findings with DESI ELGs at $z \sim 1$ are consistent with mergers triggering star formation as ELGs exhibit rapid star formation and also tend to live in close pairs and show disturbed morphology. Our results are also qualitatively consistent with [Renaud et al. \(2022\)](#)’s proposal as galactic discs should have formed at redshift $z > 2$ ([Segovia Otero et al. 2022](#)).

Ultimately, mergers and star formation are both complex processes notoriously hard to simulate. Any triggered star formation most likely depend on a plethora of properties including those of the central black holes, the molecular gas, and dynamics. DESI provides a unique window in exploring some of these relationships through its large sample size, high fidelity spectra, and broad redshift coverage. Further analyses combining DESI data and external observations in optical and radio are needed to substantiate what our findings in this paper.

11 CONCLUSIONS

ELGs are an essential cosmological tracer as we push to higher redshifts. It is imperative to understand these galaxies so that we can ensure our cosmology pipelines are robust to potential systematics in modeling ELG bias. In this paper, we improve our understanding for the ELGs and argue for the inclusion of conformity by leveraging a variety of observations and galaxy models.

First, we examine the inferred properties and the observed morphology of ELGs in COSMOS field, and we propose a physical picture where ELGs are starburst galaxies and tend to exhibit perturbed morphology. We postulate that at least a significant fraction of ELGs are undergoing mergers, which trigger star formation through gas inflow and tidal compression. This picture of merger-induced star formation also naturally gives rise to 1-halo conformity.

Next we find clear evidence for 1-halo conformity in the clustering of mock ELGs and LRGs in ILLUSTRISTNG. We also summarize existing evidence for galaxy assembly bias for ELG samples. We propose an extended ELG HOD that adopts the existing skew Gaussian+power law form, but also includes galaxy assembly bias and a flexible model for 1-halo conformity.

Then, we analyze the DESI auto and cross-correlations of the LRG and ELG samples in search of evidence of conformity in the data. We find that the DESI auto and cross-correlations favor both the inclusion of 1-halo conformity and shear-based assembly bias for the ELG HOD. However, the model preference is not conclusive based on the clustering measurements alone and we continue to find a degeneracy between small α and conformity.

In order to break this degeneracy, we directly constrain ELG satellite power index α by counting ELG satellites around redMaPPer clusters where we have estimates of halo mass from previous clustering and lensing analyses. We find that a rough α range of $0.8 < \alpha < 1.2$, which disfavors the vanilla HOD model, where $\alpha = 0.3$. We have taken a series of steps to reduce our exposure to systematics and conducted self-consistency tests to demonstrate a certain level of robustness, but a more thorough analysis is needed to quantitatively constrain α from cluster–ELG cross-correlations. Nevertheless, we find a clear positive correlation between ELG satellite number and cluster richness, rejecting models of negative α .

Furthermore, we probe the origin of ELG conformity by stress testing UniverseMachine, a flexible model that relies on the assumption that star formation only depends on individual mass assembly of the halos. We show the existing UniverseMachine model may not be flexible enough to consistently predict the stellar mass function, the SFR distribution, and the clustering of DESI ELGs. These tests also elucidate the distinction between 1-halo conformity due to triggered starburst and conformity as an emergent phenomenon of galaxy assembly bias. We argue that an extended model for star formation that introduces a secondary dependence on the halo environment is potentially needed to consistently explain all the ELG observables. Finally, we compare our studies to existing discussions of conformity and weigh in on the debate on merger–SFR connection.

While we have offered several pieces of evidence for ELG conformity and taken the first steps in understanding the nature of ELG, higher resolution spectra and detailed SED modeling are needed to better constrain the relevant galaxy properties. Additional observations that reveal detailed morphology and galaxy kinematics would also greatly help us confirm and dissect merger processes. In terms of HOD modeling, while our extended model can produce reasonably good fits, further refinements are likely needed to fully describe the observed clustering. These works are necessary not just in advancing our understanding of galaxy evolution beyond $z \sim 1$, but also in enabling robust cosmology with high-redshift large-scale structure analyses with the next generation of cosmological surveys.

ACKNOWLEDGEMENTS

We thank Wren Suess and Allison Strom for useful conversations. We thank Andrew Hearin and Yipeng Jing for constructive feedback.

This work was supported by grant DE-SC0013718 and under DE-AC02-76SF00515 to SLAC National Accelerator Laboratory, and by the Kavli Institute for Particle Astrophysics and Cosmology. MdlR was supported by a Stanford Science Fellowship at Stanford University. This work was performed in part at the Aspen Center for Physics, which is supported by National Science Foundation grant PHY-2210452.

This material is based upon work supported by the U.S. Department of Energy (DOE), Office of Science, Office of High-Energy Physics, under Contract No. DE-AC02-05CH11231, and by the National Energy Research Scientific Computing Center, a DOE Office of Science User Facility under the same contract. Additional support for DESI was provided by the U.S. National Science Foundation (NSF), Division of Astronomical Sciences under Contract No. AST-0950945 to the NSF’s National Optical-Infrared Astronomy Research Laboratory; the Science and Technology Facilities Council of the United Kingdom; the Gordon and Betty Moore Foundation; the Heising-Simons Foundation; the French Alternative Energies and Atomic Energy Commission (CEA); the National Council of Science and Technology of Mexico (CONACYT); the Ministry of Science and Innovation of Spain (MICINN), and by the DESI Member Institutions: <https://www.desi.lbl.gov/collaborating-institutions>. Any opinions, findings, and conclusions or recommendations expressed in this material are those of the author(s) and do not necessarily reflect the views of the U. S. National Science Foundation, the U. S. Department of Energy, or any of the listed funding agencies.

The authors are honored to be permitted to conduct scientific research on Iolkam Du’ag (Kitt Peak), a mountain with particular significance to the Tohono O’odham Nation.

This work made use of Astropy:³ a community-developed core Python package and an ecosystem of tools and resources for astronomy (Astropy Collaboration et al. 2013, 2018, 2022).

DATA AVAILABILITY

The simulation data are available at <https://abacussummit.readthedocs.io/en/latest/>. The ABACUSHOD code package is publicly available as a part of the ABACUSUTILS package at <https://github.com/abacusorg/abacusutils>. Example usage can be found at <https://abacusutils.readthedocs.io/en/latest/hod.html>. All mock products will be made available at <https://data.desi.lbl.gov>.

REFERENCES

- Abazajian K. N., et al., 2009, *ApJS*, 182, 543
 Abbott T. M. C., et al., 2020, *Phys. Rev. D*, 102, 023509
 Alam S., Peacock J. A., Kraljic K., Ross A. J., Comparat J., 2020, *MNRAS*, 497, 581
 Alam S., et al., 2021, *MNRAS*, 504, 4667
 Ann H. B., Park C., Choi Y.-Y., 2008, *MNRAS*, 389, 86
 Arnouts S., et al., 2002, *Mon. Not. Roy. Astron. Soc.*, 329, 355
 Artale M. C., Zehavi I., Contreras S., Norberg P., 2018, *MNRAS*, 480, 3978
 Astropy Collaboration et al., 2013, *A&A*, 558, A33
 Astropy Collaboration et al., 2018, *AJ*, 156, 123
 Astropy Collaboration et al., 2022, *apj*, 935, 167
 Avila S., et al., 2020, *MNRAS*, 499, 5486

³ <http://www.astropy.org>

- Ayromlou M., Kauffmann G., Anand A., White S. D. M., 2023, *MNRAS*, **519**, 1913
- Barnes J. E., 2004, *MNRAS*, **350**, 798
- Baxter E. J., Rozo E., Jain B., Rykoff E., Wechsler R. H., 2016, *MNRAS*, **463**, 205
- Becker M. R., 2015, *arXiv e-prints*, p. [arXiv:1507.03605](https://arxiv.org/abs/1507.03605)
- Behroozi P., Wechsler R. H., Hearin A. P., Conroy C., 2019a, *MNRAS*, **488**, 3143
- Behroozi P., Wechsler R. H., Hearin A. P., Conroy C., 2019b, *MNRAS*, **488**, 3143
- Beltz-Mohrman G. D., Szewciw A. O., Berlind A. A., Sinha M., 2023, *ApJ*, **948**, 100
- Berlind A. A., Weinberg D. H., 2002, *ApJ*, **575**, 587
- Berlind A. A., et al., 2003, *ApJ*, **593**, 1
- Berti A. M., Coil A. L., Behroozi P. S., Eisenstein D. J., Bray A. D., Cool R. J., Moustakas J., 2017, *ApJ*, **834**, 87
- Bianchi D., Percival W. J., 2017, *MNRAS*, **472**, 1106
- Blanton M. R., Berlind A. A., 2007, *ApJ*, **664**, 791
- Bose S., Eisenstein D. J., Hernquist L., Pillepich A., Nelson D., Marinacci F., Springel V., Vogelsberger M., 2019, *MNRAS*, **490**, 5693
- Bose S., et al., 2022, *arXiv e-prints*, p. [arXiv:2210.10065](https://arxiv.org/abs/2210.10065)
- Bray A. D., et al., 2016, *MNRAS*, **455**, 185
- Brinchmann J., Charlot S., White S. D. M., Tremonti C., Kauffmann G., Heckman T., Brinkmann J., 2004, *MNRAS*, **351**, 1151
- Chapman M. J., et al., 2022, *MNRAS*, **516**, 617
- Chaves-Montero J., Angulo R. E., Schaye J., Schaller M., Crain R. A., Furlong M., Theuns T., 2016, *MNRAS*, **460**, 3100
- Coil A. L., et al., 2008, *ApJ*, **672**, 153
- Conroy C., Gunn J. E., 2010, *ApJ*, **712**, 833
- Conroy C., Wechsler R. H., Kravtsov A. V., 2006, *ApJ*, **647**, 201
- Contreras S., Zehavi I., Padilla N., Baugh C. M., Jiménez E., Lacerna I., 2019, *MNRAS*, **484**, 1133
- Contreras S., Chaves-Montero J., Angulo R. E., 2023, *MNRAS*, **523**, 1
- Cooray A., Sheth R., 2002, *Phys. Rep.*, **372**, 1
- Cortijo-Ferrero C., et al., 2017, *MNRAS*, **467**, 3898
- Costanzi M., et al., 2019, *MNRAS*, **482**, 490
- Costanzi M., et al., 2021, *Phys. Rev. D*, **103**, 043522
- Cox T. J., Jonsson P., Somerville R. S., Primack J. R., Dekel A., 2008, *MNRAS*, **384**, 386
- Croton D. J., Gao L., White S. D. M., 2007, *MNRAS*, **374**, 1303
- DESI Collaboration et al., 2016, *arXiv e-prints*, p. [arXiv:1611.00036](https://arxiv.org/abs/1611.00036)
- DESI Collaboration et al., 2023a, *arXiv e-prints*, p. [arXiv:2306.06307](https://arxiv.org/abs/2306.06307)
- DESI Collaboration et al., 2023b, *arXiv e-prints*, p. [arXiv:2306.06308](https://arxiv.org/abs/2306.06308)
- Davies L. J. M., et al., 2015, *MNRAS*, **452**, 616
- Dawson K. S., et al., 2016, *AJ*, **151**, 44
- Delgado A. M., Wadekar D., Hadzhiyska B., Bose S., Hernquist L., Ho S., 2022, *MNRAS*, **515**, 2733
- Dey A., et al., 2019, *AJ*, **157**, 168
- Drinkwater M. J., et al., 2010, *MNRAS*, **401**, 1429
- Elbaz D., et al., 2018, *A&A*, **616**, A110
- Ellison S. L., Mendel J. T., Patton D. R., Scudder J. M., 2013, *MNRAS*, **435**, 3627
- Favole G., et al., 2016, *MNRAS*, **461**, 3421
- Feldman H. A., Kaiser N., Peacock J. A., 1994, *Astrophys. J.*, **426**, 23
- Fensch J., et al., 2017, *MNRAS*, **465**, 1934
- Gao L., White S. D. M., 2007, *MNRAS*, **377**, L5
- Gao L., Springel V., White S. D. M., 2005, *MNRAS*, **363**, L66
- Gao H., et al., 2023a, *arXiv e-prints*, p. [arXiv:2309.03802](https://arxiv.org/abs/2309.03802)
- Gao H., et al., 2023b, *ApJ*, **954**, 207
- Garrison L. H., Eisenstein D. J., Pinto P. A., 2019, *MNRAS*, **485**, 3370
- Garrison L. H., Eisenstein D. J., Ferrer D., Maksimova N. A., Pinto P. A., 2021, *MNRAS*, **508**, 575
- Guo H., et al., 2014, *MNRAS*, **441**, 2398
- Guo H., et al., 2015a, *MNRAS*, **446**, 578
- Guo H., et al., 2015b, *MNRAS*, **453**, 4368
- Guo H., et al., 2019, *ApJ*, **871**, 147
- Hadzhiyska B., Bose S., Eisenstein D., Hernquist L., Spergel D. N., 2020, *MNRAS*, **493**, 5506
- Hadzhiyska B., Tacchella S., Bose S., Eisenstein D. J., 2021, *MNRAS*, **502**, 3599
- Hadzhiyska B., et al., 2022a, *arXiv e-prints*, p. [arXiv:2210.10072](https://arxiv.org/abs/2210.10072)
- Hadzhiyska B., Eisenstein D., Bose S., Garrison L. H., Maksimova N., 2022b, *MNRAS*, **509**, 501
- Hartley W. G., Conselice C. J., Mortlock A., Foucaud S., Simpson C., 2015, *MNRAS*, **451**, 1613
- Hausen R., Robertson B. E., 2020, *ApJS*, **248**, 20
- Hearin A. P., Watson D. F., van den Bosch F. C., 2015, *MNRAS*, **452**, 1958
- Hearin A. P., Zentner A. R., van den Bosch F. C., Campbell D., Tollerud E., 2016a, *MNRAS*, **460**, 2552
- Hearin A. P., Behroozi P. S., van den Bosch F. C., 2016b, *MNRAS*, **461**, 2135
- Hernández-Aguayo C., et al., 2022, *arXiv e-prints*, p. [arXiv:2210.10059](https://arxiv.org/abs/2210.10059)
- Hester J. A., Tasitsiomi A., 2010, *ApJ*, **715**, 342
- Hopkins P. F., Cox T. J., Hernquist L., Narayanan D., Hayward C. C., Murray N., 2013, *MNRAS*, **430**, 1901
- Horstman K., et al., 2021, *MNRAS*, **501**, 137
- Ider Chitham J., et al., 2020, *MNRAS*, **499**, 4768
- Ilbert O., et al., 2006, *A&A*, **457**, 841
- Jiménez E., Padilla N., Contreras S., Zehavi I., Baugh C. M., Orsi Á., 2021, *MNRAS*, **506**, 3155
- Jing Y. P., Mo H. J., Börner G., 1998, *ApJ*, **494**, 1
- Kauffmann G., 2015, *MNRAS*, **454**, 1840
- Kauffmann G., et al., 2003, *MNRAS*, **341**, 33
- Kauffmann G., Li C., Zhang W., Weinmann S., 2013, *MNRAS*, **430**, 1447
- Kawinwanichakij L., et al., 2016, *ApJ*, **817**, 9
- Kennicutt Robert C. J., Keel W. C., van der Hulst J. M., Hummel E., Roettiger K. A., 1987, *AJ*, **93**, 1011
- Kim J.-h., Wise J. H., Abel T., 2009, *ApJ*, **694**, L123
- Knapen J. H., James P. A., 2009, *The Astrophysical Journal*, **698**, 1437
- Knapen J. H., Cisternas M., Querejeta M., 2015, *MNRAS*, **454**, 1742
- Knobel C., Lilly S. J., Woo J., Kovač K., 2015, *ApJ*, **800**, 24
- Kobayashi Y., Nishimichi T., Takada M., Miyatake H., 2022, *Phys. Rev. D*, **105**, 083517
- Koekemoer A. M., et al., 2007, *ApJS*, **172**, 196
- Kravtsov A. V., Berlind A. A., Wechsler R. H., Klypin A. A., Gottlöber S., Allgood B., Primack J. R., 2004, *ApJ*, **609**, 35
- Kwan J., Heitmann K., Habib S., Padmanabhan N., Lawrence E., Finkel H., Frontiere N., Pope A., 2015, *ApJ*, **810**, 35
- Lackner C. N., et al., 2014, *AJ*, **148**, 137
- Laigle C., et al., 2016, *ApJS*, **224**, 24
- Lambas D. G., Alonso S., Mesa V., O'Mill A. L., 2012, *A&A*, **539**, A45
- Landy S. D., Szalay A. S., 1993, *ApJ*, **412**, 64
- Lange J. U., Yang X., Guo H., Luo W., van den Bosch F. C., 2019a, *MNRAS*, **488**, 5771
- Lange J. U., van den Bosch F. C., Zentner A. R., Wang K., Hearin A. P., Guo H., 2019b, *MNRAS*, **490**, 1870
- Lange J. U., Hearin A. P., Leauthaud A., van den Bosch F. C., Guo H., DeRose J., 2022, *MNRAS*, **509**, 1779
- Larson R. B., Tinsley B. M., 1978, *ApJ*, **219**, 46
- Lasker J., in prep., XXX
- Lawrence A., et al., 2007, *MNRAS*, **379**, 1599
- Leja J., et al., 2019, *ApJ*, **877**, 140
- Levi M., et al., 2013a, *arXiv e-prints*, p. [arXiv:1308.0847](https://arxiv.org/abs/1308.0847)
- Levi M., et al., 2013b, *arXiv e-prints*, p. [arXiv:1308.0847](https://arxiv.org/abs/1308.0847)
- Li Y., Mo H. J., Gao L., 2008, *MNRAS*, **389**, 1419
- Lin L., et al., 2010, *ApJ*, **718**, 1158
- Linke L., Simon P., Schneider P., Farrow D. J., Rödiger J., Wright A. H., 2022, *A&A*, **665**, A38
- Luu K., 2021, *stochopy*: Python library for stochastic numerical optimization, [doi:10.5281/zenodo.5717781](https://doi.org/10.5281/zenodo.5717781), <https://doi.org/10.5281/zenodo.5717781>
- Maksimova N. A., Garrison L. H., Eisenstein D. J., Hadzhiyska B., Bose S., Satterthwaite T. P., 2021, *MNRAS*, **506**, 3155
- Mao Y.-Y., Williamson M., Wechsler R. H., 2015, *ApJ*, **810**, 21
- Marinacci F., et al., 2018, *MNRAS*, **480**, 5113
- Massey R., Stoughton C., Leauthaud A., Rhodes J., Koekemoer A., Ellis R., Shaghoulouian E., 2009, *arXiv e-prints*, p. [arXiv:0909.0507](https://arxiv.org/abs/0909.0507)

- McClintock T., et al., 2019, *MNRAS*, **482**, 1352
- Mihos J. C., Hernquist L., 1996, *ApJ*, **464**, 641
- Miyatake H., More S., Takada M., Spergel D. N., Mandelbaum R., Rykoff E. S., Rozo E., 2016, *Phys. Rev. Lett.*, **116**, 041301
- Mohammad F. G., et al., 2020, *MNRAS*, **498**, 128
- Moreno J., Torrey P., Ellison S. L., Patton D. R., Bluck A. F. L., Bansal G., Hernquist L., 2015, *MNRAS*, **448**, 1107
- Moreno J., et al., 2021, *MNRAS*, **503**, 3113
- Murata R., et al., 2019, *PASJ*, **71**, 107
- Myles J., et al., 2021, *MNRAS*, **505**, 33
- Naiman J. P., et al., 2018, *MNRAS*, **477**, 1206
- Nelson D., et al., 2018, *MNRAS*, **475**, 624
- Nelson D., et al., 2019a, *Computational Astrophysics and Cosmology*, **6**, 2
- Nelson D., et al., 2019b, *MNRAS*, **490**, 3234
- Newman J. A., et al., 2013, *ApJS*, **208**, 5
- Pahwa I., Paranjape A., 2017, *MNRAS*, **470**, 1298
- Pakmor R., et al., 2022, arXiv e-prints, p. arXiv:2210.10060
- Paranjape A., Kovač K., Hartley W. G., Pahwa I., 2015, *MNRAS*, **454**, 3030
- Parejko J. K., et al., 2013, *MNRAS*, **429**, 98
- Peacock J. A., Smith R. E., 2000, *MNRAS*, **318**, 1144
- Percival W. J., Bianchi D., 2017, *MNRAS*, **472**, L40
- Pillepich A., et al., 2018, *MNRAS*, **475**, 648
- Pillepich A., et al., 2019, *MNRAS*, **490**, 3196
- Planck Collaboration et al., 2016, *A&A*, **594**, A13
- Planck Collaboration et al., 2020, *A&A*, **641**, A6
- Prescott M., et al., 2011, *MNRAS*, **417**, 1374
- Pujol A., Gaztañaga E., 2014, *MNRAS*, **442**, 1930
- Rafieferantsoa M., Davé R., 2018, *MNRAS*, **475**, 955
- Raichoor A., et al., 2017, *MNRAS*, **471**, 3955
- Raichoor A., et al., 2020, *Research Notes of the American Astronomical Society*, **4**, 180
- Raichoor A., et al., 2023, *AJ*, **165**, 126
- Renaud F., Segovia Otero Á., Agertz O., 2022, *MNRAS*, **516**, 4922
- Rocher A., et al., 2023, arXiv e-prints, p. arXiv:2306.06319
- Rodighiero G., et al., 2011, *ApJ*, **739**, L40
- Rodríguez-Torres S. A., et al., 2016, *MNRAS*, **460**, 1173
- Ross A. J., Brunner R. J., 2009, *MNRAS*, **399**, 878
- Rossi G., et al., 2021, *MNRAS*, **505**, 377
- Roze E., Rykoff E. S., Bartlett J. G., Melin J.-B., 2015, *MNRAS*, **450**, 592
- Saitoh T. R., Daisaka H., Kokubo E., Makino J., Okamoto T., Tomisaka K., Wada K., Yoshida N., 2009, *PASJ*, **61**, 481
- Salcedo A. N., et al., 2022, *Science China Physics, Mechanics, and Astronomy*, **65**, 109811
- Sanders D. B., Soifer B. T., Elias J. H., Madore B. F., Matthews K., Neugebauer G., Scoville N. Z., 1988, *ApJ*, **325**, 74
- Schreiber C., et al., 2015, *A&A*, **575**, A74
- Soccimarro R., Sheth R. K., Hui L., Jain B., 2001, *ApJ*, **546**, 20
- Scoville N., et al., 2007, *ApJS*, **172**, 38
- Segovia Otero Á., Renaud F., Agertz O., 2022, *MNRAS*, **516**, 2272
- Simet M., McClintock T., Mandelbaum R., Rozo E., Rykoff E., Sheldon E., Wechsler R. H., 2017, *MNRAS*, **466**, 3103
- Sin L. P. T., Lilly S. J., Henriques B. M. B., 2017, *MNRAS*, **471**, 1192
- Sinha M., Garrison L. H., 2020, *MNRAS*, **491**, 3022
- Smith A., et al., 2020, *MNRAS*, **499**, 269
- Sohn J., Geller M. J., Rines K. J., Hwang H. S., Utsumi Y., Diaferio A., 2018, *ApJ*, **856**, 172
- Sorba R., Sawicki M., 2018, *MNRAS*, **476**, 1532
- Spergel D., et al., 2013, arXiv e-prints, p. arXiv:1305.5422
- Springel V., 2010, *MNRAS*, **401**, 791
- Springel V., White S. D. M., Tormen G., Kauffmann G., 2001, *Mon. Not. Roy. Astron. Soc.*, **328**, 726
- Springel V., et al., 2005, *Nature*, **435**, 629
- Springel V., et al., 2018, *MNRAS*, **475**, 676
- Sunayama T., et al., 2020, *MNRAS*, **496**, 4468
- Takada M., et al., 2014, *PASJ*, **66**, R1
- Thorpe M. D., Ellison S. L., Pan H.-A., Lin L., Patton D. R., Bluck A. F. L., Walters D., Scudder J. M., 2022, *MNRAS*, **516**, 1462
- Tinker J. L., Wetzel A. R., 2010, *ApJ*, **719**, 88
- Tinker J. L., Hahn C., Mao Y.-Y., Wetzel A. R., Conroy C., 2018, *MNRAS*, **477**, 935
- Tran K.-V. H., Moustakas J., Gonzalez A. H., Bai L., Zaritsky D., Kautsch S. J., 2008, *ApJ*, **683**, L17
- Treyer M., et al., 2018, *MNRAS*, **477**, 2684
- Urrutia T., Lacy M., Becker R., Glikman E., 2009, in Wang W., Yang Z., Luo Z., Chen Z., eds, *Astronomical Society of the Pacific Conference Series* Vol. 408, *The Starburst-AGN Connection*. p. 299
- Verrico M. E., et al., 2023, *ApJ*, **949**, 5
- Wang W., White S. D. M., 2012, *MNRAS*, **424**, 2574
- Wang Y., Nadler E. O., Mao Y.-Y., Adhikari S., Wechsler R. H., Behroozi P., 2021, *ApJ*, **915**, 116
- Wang K., Mao Y.-Y., Zentner A. R., Guo H., Lange J. U., van den Bosch F. C., Mezini L., 2022, *MNRAS*, **516**, 4003
- Watson D. F., Berlind A. A., McBride C. K., Masjedi M., 2010, *ApJ*, **709**, 115
- Weaver J. R., et al., 2022, *ApJS*, **258**, 11
- Wechsler R. H., Tinker J. L., 2018, *ARA&A*, **56**, 435
- Wechsler R. H., Zentner A. R., Bullock J. S., Kravtsov A. V., Allgood B., 2006, *ApJ*, **652**, 71
- Weinmann S. M., van den Bosch F. C., Yang X., Mo H. J., 2006, *MNRAS*, **366**, 2
- Wetzel A. R., Tinker J. L., Conroy C., 2012, *MNRAS*, **424**, 232
- White S. D. M., Rees M. J., 1978, *MNRAS*, **183**, 341
- White M., Hernquist L., Springel V., 2001, *ApJ*, **550**, L129
- Xu X., Zehavi I., Contreras S., 2021a, *MNRAS*, **502**, 3242
- Xu X., Kumar S., Zehavi I., Contreras S., 2021b, *MNRAS*, **507**, 4879
- Yu J., et al., 2023, arXiv e-prints, p. arXiv:2306.06313
- Yuan S., Hadzhiyska B., Bose S., Eisenstein D. J., Guo H., 2021a, *MNRAS*, **502**, 3582
- Yuan S., Garrison L. H., Hadzhiyska B., Bose S., Eisenstein D. J., 2021b, *MNRAS*, **510**, 3301
- Yuan S., Garrison L. H., Eisenstein D. J., Wechsler R. H., 2022a, *MNRAS*, **512**, 5793
- Yuan S., Hadzhiyska B., Bose S., Eisenstein D. J., 2022b, *MNRAS*, **512**, 5793
- Yuan S., et al., 2023, arXiv e-prints, p. arXiv:2306.06314
- Zehavi I., et al., 2005, *ApJ*, **630**, 1
- Zehavi I., et al., 2011, *ApJ*, **736**, 59
- Zehavi I., Contreras S., Padilla N., Smith N. J., Baugh C. M., Norberg P., 2018, *ApJ*, **853**, 84
- Zentner A. R., Berlind A. A., Bullock J. S., Kravtsov A. V., Wechsler R. H., 2005, *ApJ*, **624**, 505
- Zentner A. R., Hearin A. P., van den Bosch F. C., 2014, *MNRAS*, **443**, 3044
- Zhai Z., et al., 2023, *ApJ*, **948**, 99
- Zheng Z., et al., 2005, *ApJ*, **633**, 791
- Zheng Z., Coil A. L., Zehavi I., 2007, *ApJ*, **667**, 760
- Zheng Z., Zehavi I., Eisenstein D. J., Weinberg D. H., Jing Y. P., 2009, *ApJ*, **707**, 554
- Zhou R., et al., 2020, *Research Notes of the American Astronomical Society*, **4**, 181
- Zhou R., et al., 2023, *AJ*, **165**, 58
- Zhu G., Zheng Z., Lin W. P., Jing Y. P., Kang X., Gao L., 2006, *ApJ*, **639**, L5
- Zu Y., Mandelbaum R., 2018, *MNRAS*, **476**, 1637

APPENDIX A: AUTHOR AFFILIATIONS

¹Kavli Institute for Particle Astrophysics and Cosmology, Stanford University, 452 Lomita Mall, Stanford, CA 94305, USA

²SLAC National Accelerator Laboratory, 2575 Sand Hill Road, Menlo Park, CA 94025, USA

³Department of Physics, Stanford University, 382 Via Pueblo Rd, Stanford, CA 94305, USA

⁴Department of Physics & Astronomy, Amherst College, 25 East Drive, Amherst, MA 01002, USA

⁵Department of Physics, University of California, Berkeley, CA 94720, USA

⁶Université Paris-Saclay, CEA, Institut de recherche sur les lois Fondamentales de l'Univers, 91191, Gif-sur-Yvette, France

⁷Miller Institute for Basic Research in Science, University of California, Berkeley, CA 94720, USA

⁸Lawrence Berkeley National Laboratory, 1 Cyclotron Road, Berkeley, CA 94720, USA

⁹Physics Dept., Boston University, 590 Commonwealth Avenue, Boston, MA 02215, USA

¹¹Department of Physics & Astronomy, University College London, Gower Street, London, WC1E 6BT, UK

¹²Institute for Computational Cosmology, Department of Physics, Durham University, South Road, Durham DH1 3LE, UK

¹³Instituto de Física, Universidad Nacional Autónoma de México, Cd. de México C.P. 04510, México

¹⁴Departamento de Física, Universidad de los Andes, Cra. 1 No. 18A-10, Edificio Ip, CP 111711, Bogotá, Colombia

¹⁵Department of Physics, The Ohio State University, 191 West Woodruff Avenue, Columbus, OH 43210, USA

¹⁶Center for Cosmology and AstroParticle Physics, The Ohio State University, 191 West Woodruff Avenue, Columbus, OH 43210, USA

¹⁷Institut de Física d'Altes Energies (IFAE), The Barcelona Institute of Science and Technology, Campus UAB, 08193 Bellaterra Barcelona, Spain

¹⁸NSF's NOIRLab, 950 N. Cherry Ave., Tucson, AZ 85719, USA

¹⁹Institució Catalana de Recerca i Estudis Avançats, Passeig de Lluís Companys, 23, 08010 Barcelona, Spain

²⁰Department of Physics and Astronomy, Siena College, 515 Loudon Road, Loudonville, NY 12211, USA

²¹National Astronomical Observatories, Chinese Academy of Sciences, A20 Datun Rd., Chaoyang District, Beijing, 100012, P.R. China

²²Space Sciences Laboratory, University of California, Berkeley, 7 Gauss Way, Berkeley, CA 94720, USA

²³Department of Physics, Kansas State University, 116 Cardwell Hall, Manhattan, KS 66506, USA

²⁴Department of Physics and Astronomy, Sejong University, Seoul, 143-747, Korea

²⁵Centro de Investigaciones Energéticas, Medioambientales y Tecnológicas (CIEMAT), Madrid, Spain ²⁶Department of Physics, University of Michigan, Ann Arbor, MI 48109, USA

²⁷Department of Physics and Astronomy, Ohio University, Athens, OH 45701, USA

²⁸IRFU, CEA, Université Paris-Saclay, F-91191 Gif-sur-Yvette, France

This paper has been typeset from a $\text{\TeX}/\text{\LaTeX}$ file prepared by the author.